Diabatic processes and the evolution of two contrasting summer extratropical cyclones

Article

Accepted Version

Martinez-Alvarado, O. ORCID: https://orcid.org/0000-0002-5285-0379, Gray, S. L. ORCID: https://orcid.org/0000-0001-8658-362X and Methven, J. ORCID: https://orcid.org/0000-0002-7636-6872 (2016) Diabatic processes and the evolution of two contrasting summer extratropical cyclones. Monthly Weather Review, 144 (9). pp. 3251-3276. ISSN 0027-0644 doi: 10.1175/MWR-D-15-0395.1 Available at https://centaur.reading.ac.uk/65848/

To link to this article DOI: http://dx.doi.org/10.1175/MWR-D-15-0395.1

Publisher: American Meteorological Society

Diabatic processes and the evolution of two contrasting summer extratropical cyclones

Oscar Martínez-Alvarado[1,2], Suzanne L. Gray[2] and John Methven[2]
[1] National Centre for Atmospheric Science–Atmospheric Physics, United Kingdom
[2] Department of Meteorology, University of Reading, United Kingdom

June 14, 2016

Correspondence to:
Oscar Martínez-Alvarado
Department of Meteorology, University of Reading
Earley Gate, Reading, RG6 6BB, United Kingdom
E-mail: o.martinezalvarado@reading.ac.uk
Tel: +44 (0) 118 378 8951
Fax: +44 (0) 118 378 8905

Abstract

Extratropical cyclones are typically weaker and less frequent in summer as a result of differences in the background state flow and diabatic processes with respect to other seasons. Two extratropical cyclones were observed in summer 2012 with a research aircraft during the DIAMET (DIAbatic influences on Mesoscale structure in ExTratropical storms) field campaign. The first cyclone deepened only down to 995 hPa; the second cyclone deepened down to 978 hPa and formed a potential vorticity (PV) tower, a frequent signature of intense cyclones. The objectives of this article are to quantify the effects of diabatic processes and their parametrizations on cyclone dynamics. The cyclones were analyzed through numerical simulations incorporating tracers for the effects of diabatic processes on potential temperature and PV. The simulations were compared with radar rainfall observations and dropsonde measurements. It was found that the observed maximum vapor flux in the stronger cyclone was twice as strong as in the weaker cyclone; the water vapor mass flow along the warm conveyor belt of the stronger cyclone was over half that typical in winter. The model overestimated water vapor mass flow by approximately a factor of two due to deeper structure in the rearwards flow and humidity in the weaker case. An integral tracer interpretation is introduced, relating the tracers with cross-isentropic mass transport and circulation. It is shown that the circulation around the cyclone increases much more slowly than the amplitude of the diabatically-generated PV tower. This effect is explained using the PV impermeability theorem.

1 Introduction

Intense precipitation in summer over western Europe is largely associated with the passage of extratropical cyclones. Using data from the Global Precipitation Climatology Product daily precipitation dataset (Huffman et al., 2001; Adler et al., 2003) and the ECMWF ERA-Interim reanalysis product (Simmons et al., 2007; Dee et al., 2011), Hawcroft et al. (2012) determined that more than 65% of total precipitation during June–July–August is associated with extratropical cyclones over the United Kingdom, Northern Europe and Scandinavia. Heavy precipitation can have an important societal impact as it can lead to extreme weather events such as flash flooding. Water vapor condensation in the rising air also releases latent heat, which typically intensifies the ascending motion and the cyclone near the surface (e.g. Tracton, 1973; Davis, 1992; Stoelinga, 1996; Ahmadi-Givi et al., 2004; Grams et al., 2011). For example, studying a cyclone that reached its maximum intensity (based on mean sea level pressure) on 24 February 1987, Stoelinga (1996) showed that its intensity was 70% stronger as a result of coupling between baroclinic wave growth and latent heat release. Until now, studies on latent heat release and cyclone intensification have focused on Northern Hemisphere extratropical cyclones occurring mostly during winter time (December–January–February), but also during spring (March–April–May) and autumn (September–October–November). On the other hand, the importance of latent heat release, and diabatic processes in general, for the development of summer extratropical cyclones has received much less attention.

Summer extratropical cyclones are generally less frequent and weaker than their winter counterparts. In an analysis of the ERA-Interim dataset between 1989 and 2009, Čampa and Wernli (2012) showed that the central mean sea level pressure of winter cyclones in the Northern Hemisphere can be found in the range between 930 hPa and 1030 hPa, with around 45% occurring in the band between 990 hPa and 1010 hPa and 15% occurring in the lowest band between 930 hPa and 970 hPa. In contrast, Northern Hemisphere summer cyclones can be found within the same range, but 83% occur in the band between 990 hPa and 1010 hPa and only 0.2% in the lowest band between 930 hPa and 970 hPa. These differences are arguably due to differences in the environmental conditions between summer and winter. The environmental differences include different background state flows as well as higher temperature and saturation humidity, reduced ice phase and increased insolation during summer. Despite these differences it can be hypothesized that diabatic processes contribute to the intensification of summer cyclones as much as they contribute to the intensification of cyclones in winter and other seasons. Indeed, Dearden et al. (2016) showed that ice processes, such as depositional growth, sublimation and melting, are important in determining a summer cyclone's minimum central pressure and track. However, more work is needed to fully understand the importance of diabatic processes in general for cyclone intensification in summer.

This article has two objectives. The first objective is to quantify the heating (calculated as the change in potential temperature following an air parcel) produced during the occurrence of two contrasting summer extratropical cyclones and assess the effects of this heating in terms of changes to the circulation around the cyclones. In contrast to Dearden et al. (2016), the analysis is not restricted to ice processes. Instead, all the diabatic processes represented in the model by parametrization schemes are included. The second objective is to determine the contribution that each relevant parametrization scheme made to the total heating and its effects in these two cyclones. These objectives are pursued through simulations with a numerical model that requires the parametrization of convection. The model includes tracers of diabatic effects on potential temperature (e.g. Martínez-Alvarado and Plant, 2014) and potential vorticity (PV) (e.g. Stoelinga, 1996; Gray, 2006).

The two cyclones occurred during the last field campaign of the DIAMET (DIAbatic influences on Mesoscale structures in ExTratropical storms) project (Vaughan et al., 2015), which took place in the summer of 2012. Dearden et al. (2016) use the same two cases to examine the effect of ice phase microphysical processes on summer extratropical cyclones dynamics. Both cyclones developed bent-back fronts and exhibited prolonged periods of heavy frontal precipitation (Fig. 1(a,b)). Despite these similarities, the two cyclones represent two very different intensity scenarios for summer. The first cyclone reached a central pressure minimum of 995 hPa on 19 July 2012. Its central pressure places it in the most frequent cyclone category for summer cyclones over western Europe (Čampa and Wernli, 2012): five out of an average of seven annual summer cyclones that reach maximum intensity over western

Table 1: Number of cyclones over western Europe in summer (June–July–August) and winter (December–January–February) in the ERA-Interim dataset for the period between 1989 and 2009. The definition of western Europe and the frequency columns were taken from Čampa and Wernli (2012).

	Summer		Winter	
	Number of cyclones	Occurrence per year	Number of cyclones	Occurrence per year
930–970 hPa	1	0.05	33	1.65
970–990 hPa	16	0.80	64	3.20
990–1010 hPa	99	4.95	75	3.75
1010–1030 hPa	15	0.75	10	0.50
Total	131	6.55	182	9.10

Europe have a minimum sea level pressure between 990 hPa and 1010 hPa (Table 1). In contrast, the second cyclone reached a central pressure minimum of 978 hPa on 15 August 2012. Only 0.8 summer cyclones per year on average have a minimum sea level pressure between 970 hPa and 990 hPa (Table 1). Given its minimum sea level pressure, this cyclone would be more typical of winter than summer.

The rest of the article is organized as follows. The available aircraft observations, numerical model and diabatic tracers are described in Section 2; Section 3 is devoted to the comparison of the simulations with the available observations; the results are presented and discussed in Sections 4 and 5, which deal with the July and August cases, respectively, and in Section 6, which makes a comparison in terms of diabatic processes between the two cyclones; conclusions are given in Section 7.

2 Data and methods

2.1 Available aircraft observations

The cyclone on 18 July 2012 was the subject of the DIAMET Intensive Observation Period (IOP) 13 while the cyclone on 15 August 2012 was the subject of the DIAMET IOP14. Both cyclones were observed with the instruments on board the Facility for Airborne Atmospheric Measurements (FAAM) BAe146 research aircraft (Vaughan, 2011). See Vaughan et al. (2015) for a summary of the instruments, their sampling frequency and uncertainty on output parameters.

The dropsonde system is essentially the same as that described by Martínez-Alvarado et al. (2014b). In the flights discussed in this work, the average sonde spacing was limited to a minimum of 4 minutes along the flight track or 24 km at the aircraft science speed, i.e. the aircraft speed that ensures consistent instrument performance, of 100 m s^{-1}. Eight dropsondes were released at regular time intervals during both flights, between 0830 UTC and 0902 UTC 18 July 2012 during IOP13 and between 1534 UTC and 1603 UTC 15 August 2012 during IOP14.

2.2 Hindcast simulations

The simulations have been performed using the MetUM version 7.3 which is based on the so-called "New Dynamics" dynamical core (Davies et al., 2005). The model configuration, vertical and horizontal resolutions and the domain used here are the same as in Martínez-Alvarado et al. (2014b). The model description follows Martínez-Alvarado et al. (2014b) with minor modifications to accommodate details relevant to this work. The simulations have been performed on a limited-area domain corresponding to the Met Office's recently operational North-Atlantic–European domain with 600×300 grid points. The horizontal grid spacing is 0.11° (~ 12 km) in both longitude and latitude on a rotated grid centered around 52.5°N, 2.5°W. The North-Atlantic–European domain extends approximately from 30°N to 70°N in latitude and from 60°W to 40°E in longitude. The vertical coordinate is discretized in 70 vertical levels with lid around 80 km. The initial conditions were given by Met Office operational analyses valid at 1200 UTC 17 July 2012, for IOP13, and at 1800 UTC 14 August 2012, for IOP14. The lateral boundary conditions (LBCs) consisted of the Met Office operational 3-hourly LBCs valid from 0900 UTC 17 July 2012 for 72 hours, for IOP13, and from 1500 UTC 14 August 2012 for 72 hours, for IOP14.

2.3 Diabatic tracers

The MetUM has been enhanced by the inclusion of diabatic tracers of potential temperature (θ) and PV (Martínez-Alvarado et al., 2015). The description of diabatic tracers in this section is derived from Martínez-Alvarado and Plant (2014) and Martínez-Alvarado et al. (2015) with updates and additional details relevant to this work.

Diabatic tracers of θ and PV track θ and PV changes due to diabatic processes. Diabatic potential temperature tracers enable identification of the processes (including turbulent mixing and resolved advection) that bring air parcels to their current isentropic level through cross-isentropic motion. Cross-isentropic motion is interpreted as vertical motion in isentropic coordinates so that a positive change in θ indicates mean cross-isentropic ascent while a negative change in θ indicates mean cross-isentropic descent. Notice that cross-isentropic ascent does not imply an increase in height, as an air parcel can experience an increase in θ while conserving its geopotential height. Similarly, an increase in height does not imply cross-isentropic ascent as an air parcel can ascend adiabatically. Diabatic PV tracers enable identification of modifications to the circulation and stability and the diabatic processes responsible for such modifications. Diabatic θ tracers have been previously described in Martínez-Alvarado and Plant (2014) and Martínez-Alvarado et al. (2014b), while the diabatic PV tracer technique has been developed by in Stoelinga (1996), Gray (2006), Chagnon and Gray (2009), Chagnon et al. (2013), Chagnon and Gray (2015) and Saffin et al. (2015). The diabatic tracers described here are conceptually related to those described by Cavallo and Hakim (2009) and Joos and Wernli (2012). However, those methods analyse Lagrangian tendencies whereas diabatic tracers can be interpreted as time integrals of diabatic tendencies along trajectories. Diabatic tracers of θ and PV have been used together in the analysis of forecast errors in upper-level Rossby waves (Martínez-Alvarado et al., 2015).

The idea behind diabatic tracers of θ and PV consists of the separation of the variable of interest φ (representing either θ or PV) into the sum of a materially-conserved component, φ_0, a diabatically-generated component, φ_d, and a residual, r_φ, i.e.

$$\varphi(\boldsymbol{x}, t) = \varphi_0(\boldsymbol{x}, t) + \varphi_\mathrm{d}(\boldsymbol{x}, t) + r_\varphi(\boldsymbol{x}, t), \tag{1}$$

where $\boldsymbol{x}$ represents spatial location and t is time. The materially-conserved and the diabatically-generated parts are governed by the following equations

$$\frac{D\varphi_0}{Dt} = 0 \tag{2}$$

$$\frac{D\varphi_\mathrm{d}}{Dt} = S_\varphi, \tag{3}$$

where S_φ represents a source due to diabatic processes,

$$\frac{D}{Dt} = \frac{\partial}{\partial t} + \boldsymbol{u} \cdot \nabla,$$

and $\boldsymbol{u} = (u, v, w)$ is the three-dimensional velocity field. In other words, φ_0 is unaffected by diabatic processes, and therefore conserved following an air parcel, while φ_d is affected by diabatic processes. Since φ_0 is only affected by advection, this tracer has also been called an *advection-only* tracer in other works (Chagnon et al., 2013; Chagnon and Gray, 2015; Saffin et al., 2015). The sum of (2) and (3) yields the full evolution equation for φ, under the assumption of a small residual. At initialisation time, t_0, $\varphi_0(\boldsymbol{x}, t_0) = \varphi(\boldsymbol{x}, t_0)$ and $\varphi_\mathrm{d}(\boldsymbol{x}, t_0) = 0$. The boundary conditions for φ_0 are the boundary conditions for φ while the values of φ_d are set to zero in the boundary.

Diabatic tracers can be further extended to the analysis of individual diabatic processes by separating φ_d into a series of tracers φ_p

$$\varphi_\mathrm{d} = \sum_{p \in \{\mathrm{proc}\}} \varphi_p, \tag{4}$$

where {proc} is the set of parametrized diabatic processes in the model. In this work we consider contributions from four parametrized processes, namely (i) boundary layer (BL) and turbulent mixing processes, (ii) convection, (iii) cloud microphysics and (iv) radiation. The term cloud microphysics is used here to refer to two parametrizations, namely the large-scale cloud parametrization and the large-scale precipitation parametrization. The latter includes the following microphysical processes (Wilson and Ballard, 1999): fall of ice from one layer to the next, homogeneous nucleation of ice from liquid, heterogeneous nucleation of ice from liquid or vapor, depositional growth/evaporation of ice from liquid or vapor, riming of liquid by ice, capture of raindrops by ice, evaporation of melting ice, melting of ice to rain, evaporation of rain, accretion of liquid water droplets by rain and autoconversion of liquid cloud water to rain. The contribution from gravity wave drag to the modification of PV has also been computed, but is much smaller in comparison with processes (i)–(iv) and therefore is not shown. Each tracer is selectively affected by the p-th parametrized process and governed by the equation

$$\frac{D\varphi_p}{Dt} = S_{\varphi,p}, \tag{5}$$

where $S_{\varphi,p}$ represents the source due to the p-th parametrized process so that

$$S_\varphi = \sum_{p\in\{\text{proc}\}} S_{\varphi,p}. \tag{6}$$

Equations (2), (3) and (5) are solved using the same numerical methods implemented in the MetUM to solve the evolution equations of the model's prognostic variables (velocity components, θ and moisture variables) (cf. Davies et al., 2005). However, there are details in the numerical representation of the equations of motion which have been specifically designed for the prognostic variables. These details include the staggered distribution of the variables on the Arakawa C-grid, which imply differences in the advection of PV computed from prognostic variables and as a tracer (Whitehead et al., 2014), or the treatment of the advection of θ (Davies et al., 2005). These details lead to an unavoidable mismatch between the advection of φ and that of the sum $\varphi_0+\varphi_{\mathrm{d}}$ in (1). This mismatch gives rise to the residual term in that equation. The residual grows over time in both cases, but at a slower rate for the θ tracers than for PV tracers. However, restricting the length of the simulations to less than 24 hours also restricts the residual growth. For more details regarding the growth of the residual in PV tracers the reader is referred to Saffin et al. (2015).

2.4 Integral interpretation of θ tracers: Cross-isentropic mass transport

Given that the θ_0 tracer is materially-conserved and represents the θ field at the start of the simulation, it can be used as a Lagrangian label for the vertical position (in isentropic coordinates) of air masses at the start of the simulation. An integral interpretation of the θ tracers can be achieved by analyzing the evolution of the θ_0 tracer within volumes around the cyclones' centers defined by minimum mean sea level pressure. At each considered time, the grid points within a 1000-km radius cylinder centered at the cyclone's center were classified according to their θ_0-value into seven 10-K width bins with centers at $\theta_0 = 275 + 10k$ [K] for $k = 0, 1, \ldots, 6$. This operation produces a population of grid points for each θ_0-bin, which can then be analyzed separately. The θ_0 distributions were computed hourly from the first hour of each simulation until the end of each simulation (i.e. 21 hours). This methodology is applied in Section 66.1 to determine the net heating experienced by air in each θ_0-bin, and the contributions from individual diabatic processes to these changes, as a function of time in each cyclone.

2.5 Integral interpretation of PV tracers: Circulation

Ertel PV is defined as (e.g. Haynes and McIntyre, 1987)

$$Q = \frac{1}{\rho} \nabla \times \boldsymbol{u}_{\mathrm{a}} \cdot \nabla \theta, \tag{7}$$

where ρ is density, $\boldsymbol{u}_{\mathrm{a}} = \boldsymbol{\Omega} \times \boldsymbol{r} + \boldsymbol{u}$ is the three-dimensional absolute velocity with $\boldsymbol{r}$ being a position vector from the Earth's center and $\boldsymbol{\Omega}$ being the planetary angular velocity, and ∇ is the gradient operator in geographic coordinates. The absolute circulation on an isentropic surface is given by

$$C_\theta = \oint_C \boldsymbol{u}_{\mathrm{a}} \cdot d\boldsymbol{l} = \int_R \nabla \times \boldsymbol{u}_{\mathrm{a}} \cdot \boldsymbol{k}_\theta \, dS, \tag{8}$$

where C is a closed contour on the isentropic surface enclosing region R, $d\boldsymbol{l}$ is a line element on contour C, dS is a surface element on region R and $\boldsymbol{k}_\theta$ is a unit vector normal to the isentropic surface. $\boldsymbol{k}_\theta$ can be written in terms of $\nabla\theta$ as

$$\boldsymbol{k}_\theta = \frac{\nabla\theta}{|\nabla\theta|}, \tag{9}$$

while dS is given by

$$dS = \left(\frac{\partial\theta}{\partial z}\right)^{-1} |\nabla\theta| \, dx \, dy, \tag{10}$$

where $dx\,dy$ is the projection of area element dS onto the horizontal and z is geopotential height. This expression is valid as long as θ is a monotonically increasing function of height. Substituting (9) and (10) into (8) yields

$$C_\theta = \int_R \left(\frac{\partial\theta}{\partial z}\right)^{-1} \nabla \times \boldsymbol{u}_{\mathrm{a}} \cdot \nabla\theta \, dx \, dy. \tag{11}$$

Using (7) and defining the isentropic density as

$$\sigma = \rho \left(\frac{\partial\theta}{\partial z}\right)^{-1}, \tag{12}$$

we can write

$$C_\theta = \int_R \sigma \, Q \, dxdy. \tag{13}$$

Using (1) PV can be written as

$$Q = Q_0 + Q_{\mathrm{d}} + r_Q, \tag{14}$$

where Q_0, Q_{d} and r_Q are the materially-conserved, the diabatically-generated and the residual parts of PV, respectively. Multiplying (14) by σ and integrating over the isentropic region R

we obtain

$$C_\theta = C_0 + C_\mathrm{d} + C_\mathrm{r}, \tag{15}$$

where

$$C_0 = \int_R \sigma\, Q_0 dx\, dy \quad \text{and} \quad C_\mathrm{d} = \int_R \sigma\, Q_\mathrm{d} dx\, dy, \tag{16}$$

i.e. C_0 and C_d are contributions to the circulation on isentropic surfaces that can be directly associated with the materially-conserved and the diabatically-generated parts of PV. The contribution associated with the residual is assumed small, given that the duration of the simulations is limited to satisfy this condition, but can be computed as $C_\mathrm{r} = C_\theta - (C_0 + C_\mathrm{d})$. Dividing (15) by $\int_R dx\, dy$ we obtain

$$\zeta_\theta = \zeta_{\theta,0} + \zeta_{\theta,\mathrm{d}} + \zeta_{\theta,\mathrm{r}}, \tag{17}$$

where ζ_θ is area-averaged isentropic vorticity, $\zeta_{\theta,0}$ and $\zeta_{\theta,\mathrm{d}}$ are the contributions associated with the materially-conserved and diabatically-generated parts of PV, respectively, and $\zeta_{\theta,\mathrm{r}}$ is the contribution associated with r_Q. These results are valid for any isentropic surface. However, the computations can be carried out for a set of isentropic levels at different time steps to construct time series of vertical profiles for ζ_θ, $\zeta_{\theta,0}$ and $\zeta_{\theta,\mathrm{d}}$, as is done in Section 66.1.

3 Comparison between simulations and observations

The two extratropical cyclones in this study exhibited similarities. The IOP13 cyclone travelled around 600 km during 18 July 2012; the IOP14 cyclone travelled around 700 km during 15 August 2012. Furthermore, both cyclones produced precipitation for prolonged periods. Precipitation associated with the IOP13 cyclone started around 1800 UTC 17 July 2012 over Northern Ireland and ended at around 0100 UTC 19 July 2012 across northern England. Radar rainfall rates at 0900 UTC 18 July 2012 show heavy precipitation on a band over Scotland, corresponding to the detached warm front, and scattered precipitation over the south-west of England, corresponding to weak precipitation at the cold front (Fig. 1a). Precipitation associated with the IOP14 cyclone started before 0000 UTC 15 August 2012 and continued until the end of the day, passing over the United Kingdom and Ireland from south to north (Fig. 1b). These features were well represented by the simulations. Figure 1c shows the rainfall rate for IOP13 derived from the simulation corresponding to the time shown in Fig. 1a (i.e. T+21). Figure 1d shows the corresponding rainfall rate for IOP14 for the time shown in Fig. 1b (i.e. T+22). In both cases, the simulations compare well with radar observations in terms of location and intensity of precipitating features, bar differences in the resolutions of both datasets. However, one feature that the model fails to represent is the clear split into two precipitation bands over the east of England in IOP14 due to the gap between the system's cold and warm fronts (Fig. 1b) even though the model is able to represent the gap in the equivalent potential temperature, θ_e, field.

Despite the similarities in speed and precipitation, the cyclones represent very different synoptic conditions. The synoptic chart for IOP13 at 0600 UTC 19 July 2012 shows a T-bone structure (Shapiro and Keyser, 1990) (Fig. 1e). The IOP13 cyclone was a shallow system that deepened slightly after the time shown, reaching 995 hPa at 0600 UTC 19 July 2012. However, its structure remained largely the same from 0600 UTC 18 July 2012 until the end of its life cycle. In contrast, the IOP14 cyclone was a relatively deep system for a summer cyclone. Figure 1f shows the IOP14 cyclone at 1200 UTC 15 August 2012 with its bent-back front (analyzed as an occluded front) wrapped up around the system's low-pressure center. These features were also well represented by the simulations as indicated by the 850-hPa θ_e isolines, in Figs. 1(c,d) (Notice that there is a three-hour mismatch between Figs. 1(a,c) and 1e and a four-hour mismatch between Figs. 1(b,d) and 1f). Further comparisons between the simulation and operational Met Office analysis charts were performed in terms of cyclone position and intensity (central pressure). For IOP13, during the interval between 1800 UTC 17 July 2012 and 1200 UTC 18 July 2012 inclusive, the maximum position error is 151 km while the maximum error in minimum sea level pressure is 4 hPa. For IOP14, during the interval between 0000 UTC and 1800 UTC 15 August 2012 inclusive, the maximum position error is 218 km while the maximum error in minimum sea level pressure is 11 hPa. The cyclone in IOP14 deepens at a faster rate in the simulation than in analysis at the beginning of the study period. In spite of this, the simulations can be considered a realistic representation of the development of both cyclones.

Several quantities derived from the dropsonde observations during the first IOP13 leg are shown in a vertical cross section in Figs. 2(a,c). Figure 2a shows zonal velocity, u, θ and relative humidity with respect to ice, $\mathrm{RH_{ice}}$; Fig. 2c shows θ_e and water vapor flux defined as $\phi_q = \rho q v_H$, where q is specific humidity and v_H is the horizontal wind component across the section. Easterly winds of more than 10 m s^{-1}, constituting the system's cold conveyor belt (CCB), are confined below 900 hPa. These winds are located around 57.5°N within a region of strong horizontal θ_e gradient, which corresponds to the system's warm front (Fig. 2c). Westerly winds of similar magnitude, located south of the warm front, extend to pressures as low as 650 hPa. The system's warm conveyor belt (WCB) is located around 400 hPa. The CCB and WCB have been identified by their position relative to the cyclone's center and surface fronts. A column with $\mathrm{RH_{ice}} > 90\%$ extends from the surface to pressures around 450 hPa. The maximum westward ϕ_q is confined below 900 hPa within the warm front region, between 57°N and 58°N. Considering only ϕ_q with a westward component in Fig. 2c (i.e. $\phi_q < 0$) produces a total water vapor mass flow across the vertical dropsonde curtain below 7 km ($\sim$ 400 hPa) of $\Phi_{q,\mathrm{IOP13}} = 1.99 \times 10^7$ kg s^{-1}.

Figures 2(b,d) show vertical sections through segment A–B (Fig. 1c) for the same quantities as in Figs. 2(a,c), but derived from the simulation at 0900 UTC 18 July 2012 (T+21). Segment A–B approximately corresponds to the aircraft's track during the first IOP13 dropsonde leg. Zonal velocity has similar magnitude in model and observations (Fig. 2b). However, the system's CCB extends further up in the model than in observations, reaching 850 hPa. The column with $\mathrm{RH_{ice}} > 90\%$ also extends higher in the model than in observations, indicating that the model's atmosphere is too moist. This wet bias is a deficiency that has been previously identified in other studies using the MetUM version 7.3 (e.g Martínez-Alvarado et al., 2014a). A systematic wet bias in a model could be leading to an overestimation of WCB intensities and outflow levels as well as tropopause height (Schäfler and Harnisch, 2015). Furthermore, Joos and Wernli (2012) showed that evaporation of rain contributes to low-level PV modification. Therefore, the evaporation in unsaturated air and hence the low-level diabatic PV modification might be underestimated by a model exhibiting a wet bias; however, it is not possible to quantify these effects with the available observations. The position of the warm front is similar in model and observations (Fig. 2d). The gradient of θ_e appears stronger in the model, especially below 800 hPa. However, this apparent difference is due to the spacing of dropsondes. Analysis of in-situ observations during a transect flight through the front suggests that the front width was approximately 25 km with a velocity step at the lowest flight level ($\sim$ 957 hPa) of 12 m s^{-1} (i.e. an horizontal shear of 5×10^{-4} s^{-1}). The vertical structure of ϕ_q is also similar in model and observations. The maximum ϕ_q with a westward component is located within the region of maximum θ_e gradient and confined below 900 hPa (Fig. 2d). However, its magnitude is around 50% stronger in the model than in observations, as a result of stronger u and higher moisture in the model than in observations. Thus, $\Phi_{q,\mathrm{IOP13,sim}} = 4.40 \times 10^7$ kg s^{-1} according to the model, i.e. more than twice as much as in the observations.

Now we compare the dropsonde observations obtained during IOP14 with the simulation at 1600 UTC 15 July 2012 (T+22). The vertical structure of dropsonde-derived u, θ and RH$_{\mathrm{ice}}$ is shown in Fig. 3a while that of ϕ_q and θ_e is shown in Fig. 3c. In this case, the flow moves westwards across the whole dropsonde curtain (Fig. 3a). The maximum zonal velocity ($|u| > 30$ m s^{-1}) is located at mid-tropospheric levels around 450 hPa, constituting the system's WCB. At lower levels, the maximum zonal velocity ($|u| > 20$ m s^{-1}) is located within a low-level jet (LLJ) towards the section's northern edge behind the system's cold front. The cold front is located around 55.5°N near the surface. A column with RH$_{\mathrm{ice}} > 90\%$ extends over the cold front to the upper part of the vertical section (Fig. 3a). In this case, ϕ_q exhibits maximum intensity ($|\phi_q| > 0.25$ kg m^{-2} s^{-1}) towards the section's northern edge (Fig. 3c). This flux produces a water vapor mass flow with a westward component across the vertical curtain below 7 km of $\Phi_{q,\mathrm{IOP14}} = 1.17 \times 10^8$ kg s^{-1}. This value is comparable in magnitude to the typical meridional water vapor mass flow in a Northern Hemisphere atmospheric river $\Phi_{q,\mathrm{AR}} = 2.2 \times 10^8$ kg s^{-1} (Zhu and Newell, 1998). Figure 3 also shows vertical sections for model-derived variables through segment C–D (Fig. 1d), which corresponds to the aircraft's track during the IOP14 dropsonde leg. In the model, the LLJ core ($|u| > 25$ m s^{-1}) appears in the section around 55.5°N confined below 800 hPa (Fig. 3b). Like in IOP13, the column with RH$_{\mathrm{ice}} > 90\%$ spans a larger area within the section in the model than in the observations. However, in this case, this can be due to a mismatch between the position of the system's cold front, which in the model is located further south (around 54.5°N) than in the observations. The maximum vapor flux in IOP14 is twice as strong as in IOP13 in both observations and simulations.

4 Diabatic effects in IOP13

Figure 4 shows θ_0 and 2-PVU contours in IOP13 on the 319-K and 305-K isentropic levels to illustrate the synoptic situation at upper and lower levels, respectively. On the 319-K isentropic level (Fig. 4a) the 2-PVU contour represents the intersection of the isentropic surface with the tropopause. Thus, in this figure, the isentropic surface is in stratospheric air over Ireland and part of Great Britain and tropospheric air over the south of England and the north of Scotland. On this isentropic level, there is a band of strong cross-isentropic ascent spanning a sector from the north-west to the east-south-east of the cyclone center. This band of cross-isentropic ascent corresponds to the system's WCB outflow. The air mass constituting the WCB outflow was located within the boundary layer (BL), at levels with $\theta_0 < 290$ K, at the start of the simulation. However, most of the cross-isentropically ascending air originates within the lower and middle free troposphere (above the BL), from the layer $290 < \theta_0 < 319$ [K]. Outside the WCB outflow region, cross-isentropic subsidence is found not only in the stratospheric region that constitutes the descending air within the dry intrusion to the south and west of the cyclone center, but through most of the troposphere as well. The average cross-isentropic subsidence corresponds to an average cooling rate of 1.3 $\mathrm{K\,day^{-1}}$, which is consistent with radiative cooling (Haynes et al., 2013). On the 305-K isentropic level (Fig. 4b) the 2-PVU contour represents low-level positive PV anomalies, which are of diabatic origin, as will be shown later in this and the next Sections. One such an anomaly, shaped as an elongated east-west strip, is located immediately to the north of the cyclone's center. On this isentropic level, cross-isentropic ascent predominates to the north of the cyclone center. This region of cross-isentropic ascent is located over the system's warm front and is therefore the lower portion of the cross-isentropically ascending WCB in Fig. 4a.

Figure 5 shows θ_0 and diabatically-generated PV on vertical sections along segment E–F in Fig. 4, which is a north–south cross section through the cyclone's center. The figure also shows 2-PVU contours and θ contours to allow comparison with Fig. 4. Figure 6 shows the partition of diabatic PV into contributions from parametrized processes in IOP13, as well as contours for PV = 2 PVU and θ to facilitate comparisons with Figs. 4–5. There are three regions in the cross sections that deserve comment, namely the system's WCB, low-level PV anomalies and the region close to the tropopause.

A deep column of air originating from the layer $290 < \theta_0 < 300$ [K] extends from around 700 hPa up to the upper troposphere at around 300 hPa (320 K). At low levels it is flanked to the south by the system's cold front, which by this time is already occluded, and to the north by the system's warm front (Fig. 5a). Comparisons of the intersections of this column with the 305-K and 319-K isentropic surfaces with those shown in Fig. 4 confirm that this is part of the system's WCB, which constitutes the cyclone's air stream that has experienced the most intense heating.

The low-level positive PV anomaly, which in the 305-K isentropic surface appears as an elongated east–west feature, extends from the surface up to at least the 310-K isentropic level (500-hPa isobaric level) in this section. This low-level PV anomaly has been diabatically generated. Figure 5b shows that the PV within the anomaly has increased by more than 2 PVU due to diabatic activity. The lower part of the low-level PV anomaly (below 750 hPa) exhibits negligible θ change (Fig. 5a). Yet, it shows strong changes in PV due to BL and turbulent mixing processes (Fig. 6a). This part of the low-level PV anomaly is constituted by air that, moving quasi-isentropically, has travelled through the regions of PV production induced by BL heating (since $\dot{Q} \sim \partial\dot{\theta}/\partial z$, where $\dot{Q}$ and $\dot{\theta}$ are the material rate of change of Q and θ, respectively (e.g. Pedlosky, 1986; Stoelinga, 1996)). The upper part of the low-level PV anomaly (above 750 hPa) exhibits a small but positive θ change in the interval $0 < \Delta\theta \leq 10$ [K] (Fig. 5a). The analysis of the contribution to θ changes due to diabatic processes shows that this part of the low-level PV anomaly is constituted by air that ascended cross-isentropically due to BL processes. The cross-isentropic ascent was weakened by cooling cloud microphysical processes, such as the evaporation of cloud droplets and rain found by Dearden et al. (2016) in independent simulations of the same system to be the main cooling microphysical processes below 5 km ($\sim$ 650 hPa). The PV was modified as the cross-isentropically ascending air travelled through regions of PV production induced earlier by BL and turbulent mixing processes (Fig. 6a) and later by cloud microphysical processes taking place inside the WCB cloud (Fig. 6c). The evaporation of cloud droplets and rain can be hypothesized as responsible for the PV changes do to microphysical processes, an interpretation that is also consistent with the findings of Joos and Wernli (2012).

There are also shallow low-level regions of positive diabatically-generated PV below 800 hPa, particularly visible to the north of 58°N (Fig. 5b). These regions of positive diabatically-generated PV are generated by radiative cooling due to low-level clouds at the BL top. Radiative cooling in these regions produces cross-isentropic descent. Moreover, it destabilizes clouds and triggers BL and mixing processes, which tend to increase θ (Fu et al., 1995). The effects on PV induced by radiation have greater magnitude than those induced by BL processes so that the net effect in the final diabatically-generated PV is a dipole structure with positive on top of negative diabatically-generated PV (see Fig. 5b).

The upper troposphere is characterized by a PV reduction spanning a large section between 52°N and 59°N and between 310 K and 322 K (Fig. 5b). The region north of 56°N, between 315 K and 325 K, exhibits strong θ change in the interval $0 < \Delta\theta \leq 40$ [K] (Fig. 5a). This region is located within the WCB outflow. The PV modification is primarily due to BL and turbulent mixing processes (Fig. 6a) and occurred as cross-isentropically ascending air travelled through regions of negative PV production induced by heating within the BL and turbulent mixing in the free troposphere. Cloud microphysical processes modulated the final PV modification by inducing PV production below regions of strong latent heat release within the WCB cloud (Fig. 6c). The negative PV change directly beneath the tropopause to the south of 56°N, behind the system's cold front, is associated with post-frontal convective activity. The region south of 56°N, between 312.5 K and 317.5 K, exhibits negligible θ change (Fig. 5a). Thus, this region of negative PV modification is constituted by air that travelled quasi-isentropically through regions of negative PV production induced by heating due to post-frontal convection (Fig. 6b) and radiative cooling at cloud top level (Fig. 6d). There is also a contribution from cloud microphysics (Fig. 6c) possibly induced by the heating produced by forced vertical motion over the system's cold front to the south of the cyclone's center.

5 Diabatic effects in IOP14

Figure 7 shows θ_0 around the IOP14 cyclone center and the 2-PVU contours on two isentropic levels located at 320 K and 305 K to illustrate the synoptic situation at upper and lower levels, respectively. The intersection of the tropopause and the 320-K isentropic surface consists of a very distorted curve, as both tropospheric and stratospheric air masses have been stretched to form thin air strips spiraling around the cyclone's center (Fig. 7a). Just as in IOP13, the main feature on this level in terms of cross-isentropic ascent is the outflow of the system's WCB. The WCB typically splits into two distinct branches (Browning and Roberts, 1994); the WCB split in IOP14 can be seen in Fig. 7a. One WCB branch turns anticyclonically, forming the primary WCB (WCB1, Browning and Roberts, 1994). This branch undergoes strong cross-isentropic ascent as it is subject to strong heating (Martínez-Alvarado et al., 2014b). The secondary branch (WCB2) turns cyclonically wrapping around the cyclone's center (Browning and Roberts, 1994). This branch undergoes weaker cross-isentropic ascent than WCB1, as it is subject to less heating (Martínez-Alvarado et al., 2014b). In IOP14, there is a tropospheric air mass, located west of 20°W, which has experienced very strong cross-isentropic ascent originating from very low isentropic levels ($270 < \theta_0 < 310$ [K]). This air mass constitutes the system's WCB1 outflow. The system's WCB2 outflow consists of a distinct air mass that has undergone weaker cross-isentropic ascent, mainly originating within the layer $290 < \theta_0 < 320$ [K]. The dry intrusion in IOP14 consists of a long strip of stratospheric air that has been subject to weak cross-isentropic descent. IOP14 also exhibited low-level PV anomalies (Fig. 7b). These PV anomalies have a different structure to those in IOP13 (cf. Fig. 4b). Whereas IOP13 exhibited only one distinct low-level PV anomaly, IOP14 exhibits a series of low-level PV anomalies, forming a broken strip that spirals into the cyclone's center. Even though the cross-isentropic ascent and descent at lower levels are both weaker than at upper levels, the general spiral structure can also be easily discerned in the θ_0 tracer on the 305-K isentropic level.

Figure 8 shows θ_0, total diabatically-generated PV and 2-PVU contours on vertical sections along segment G–H in Fig. 7. Like segment E–F in Fig. 4, segment G–H is a cross-section through the cyclone's center, allowing a comparison between the two systems. Figure 9 shows the contributions to the modification of PV in IOP14 from the four parametrized processes considered here, as well as contours of PV = 2 PVU and θ to facilitate comparison with

Figs. 7 and 8.

The cross-isentropic mass transport in IOP14 is much more complex than that in IOP13 (cf. Fig. 5a). Unlike IOP13, in which there was only one main column of strong cross-isentropic ascent, strong cross-isentropic ascent occurs in at least four columns throughout the cross section in IOP14. A comparison between the intersection of the columns of cross-isentropically ascending air intersecting the 320-K isentropic level and the structures shown in Fig. 7 suggests that these columns are all part of the same air stream. This air stream corresponds to the system's WCB, whose secondary branch, WCB2, was tightly wrapped around the cyclone's center by this time (labelled C1–C2–C3 following the WCB2 spiral). The highest column of cross-isentropic ascent (labelled C1 in Fig 8) is located around 54°N. Column C1 extends from around 800 hPa (300 K) up to the upper troposphere, which by this time is located around 200 hPa (335 K). The diabatically-generated PV within this column is characterized by a core of positive diabatically-generated PV along the ascending axis over 54°N, extending from 900 hPa to around 380 hPa (Fig 8b). The core of positive PV is surrounded by negative diabatically-generated PV from 600 hPa to tropopause level (around 200 hPa). Column C1 is part of the WCB before the split; two smaller columns (labelled C2 and C3 in Fig 8), located south of 54°N, are part of WCB2. The column tops for columns C1 and C2 are also close to the local tropopause and their diabatically-generated PV structure resemble that of column C1's.

The air within the principal ascending branch of the system's WCB (column C1 in Fig. 8) produces similar PV patterns to those produced by the WCB in IOP13. The parametrization of BL processes and mixing is the main parametrization responsible for the negative diabatically-generated PV in the upper troposphere within this air stream (Fig. 9a). However, in this case the negative diabatically-generated PV is largely compensated by positive diabatically-generated PV due to the cloud microphysics parametrization (Fig. 9c), which indicates stronger heating due to this parametrization in IOP14 than in IOP13. Thus, the core of positive diabatically-generated PV over 54°N is formed by BL process at lower levels (below 500 hPa) and by cloud microphysical processes at upper levels (above 500 hPa). Dearden et al. (2016) have found, via independent simulations of this same case, that at these levels the heat released during vapor growth of ice within the WCB is a major factor in the creation of positive PV anomalies. The induction of PV sources and sinks due to the representation of latent heat release in the convection parametrization is a secondary contributor to the negative PV production at upper levels.

A column directly above the cyclone's center (labelled C4 in Fig 8) has a different structure to that of C1, C2 and C3 previously described. This column, characterised by high PV values which extend the 2-PVU contour from tropopause level to the surface, constitutes a PV tower (Rossa et al., 2000). The PV tower exhibits intense positive PV modification in its lower part (below 315 K) and negative PV modification in its upper part (Fig. 8b). A PV tower is typically composed of air from three different regions: tropopause-level air, low-level warm-sector air and low-level cold-conveyor-belt air (Rossa et al., 2000). The air comprising each of these sources has a particular heating and diabatic PV evolution (Rossa et al., 2000). The following interpretation is based on the findings by Rossa et al. (2000).

The air from tropopause level entering the PV tower, located above 400 hPa in Fig. 8a, exhibits negligible θ change, which can be inferred by comparing the θ_0 tracer versus the θ field within the PV tower. This indicates that the air has traveled quasi-isentropically, experiencing weak PV reduction along its path. Parametrized processes contribute small negative PV modification to make up the total negative diabatically-generated PV (especially noticeable around 275 hPa in Fig. 8b).

The warm-sector air entering the PV tower, located towards the northern flank of the PV tower between 700 hPa and 450 hPa in Fig. 8a, has undergone cross-isentropic ascent mainly as a result of heating and mixing within the BL, but with contribution from the convection parametrization. As the air ascended cross-isentropically through the BL, the cloud microphysics parametrization produced a small negative contribution to the θ change (not shown). The positive PV change is driven by BL and turbulent mixing processes (Fig. 9a) and heating due to the convection parametrization (Fig. 9b). However, there is also a negative contribution induced by radiative cooling taking place in clouds at BL top level (Fig. 9d).

The air moving within the system's CCB into the PV tower, being drier and colder than that from the warm sector, also experiences less cross-isentropic ascent than the warm-sector air. This air mass corresponds to the southern flank of the PV tower between 700 hPa and 450 hPa in Fig. 8a. Like for the warm-sector air, BL and mixing processes drive cross-isentropic ascent, while cloud microphysics tends to counteract this ascent by cooling the air as it ascends cross-isentropically through the BL. However, the magnitude of BL net heating is weaker in the cold-conveyor-belt air than in the warm-sector air. Another important difference between the warm-sector air and that of the cold-conveyor-belt air is given by the contribution to heating from the convection parametrization, which in the latter is negligible. The PV increased as the CCB air within the PV tower travelled through regions of PV production induced by heating due to cloud microphysical processes (Fig. 9c). However, this air also travelled through regions of negative PV production induced by BL and mixing processes (Fig. 9a).

6 Cyclone comparison

The results presented so far are restricted to the selected horizontal and vertical sections. A more thorough comparison is achieved by the integral diagnostics within cylindrical volumes centered on the cyclones under comparison. The results from such integral diagnostics, formulated around the diabatic tracers, are presented in the following two sections.

6.1 Cross-isentropic mass transport

In this section θ_0 distributions are computed following the method described in Section 22.4. The results are shown in Fig. 10(a,b), in which each color segment in the color bar represents a θ_0-bin, i.e. the isentropic layer from which air originates. There are three lines for each color segment. These lines represent the 2.5^{th} (dashed), 50^{th} (bold) and 97.5^{th} (thin) percentiles of θ values found at grid points falling within each θ_0-bin, as functions of time. By definition, the bands do not overlap at $t = 0$ since $\theta = \theta_0$ then. These percentiles are used to describe the evolution of each θ_0 distribution. The medians illustrate the strong stratification expected when averaging over these length scales ($\mathcal{O}(1000$ km)).

The minimum θ value in each cyclone illustrates a major difference between the environments of these cyclones: IOP13 evolves in an environment around 10 K colder than does IOP14, which also implies the potential for greater moisture availability near the surface in IOP14, consistent with the findings by Madonna et al. (2014), even though the actual amount of moisture available also depends on surface moisture fluxes and lapse rate. The location of the 2.5th and 97.5th percentiles essentially determine the range of the θ_0 distributions. There are layers in both cyclones that are largely isentropic, for which the 2.5th and 97.5th percentiles stay at the same θ values. These are located at upper levels, above 320 K in IOP13 and above 330 K in IOP14, corresponding to stratospheric layers. The difference in the vertical locations of these largely isentropic layers is consistent with the differences in tropopause height suggested by the vertical sections in Figs. 5 and 8. The most important differences between the cyclones are described by the 97.5th-percentile lines. Both cyclones exhibit a certain degree of cross-isentropic ascent throughout the 21-h period. In IOP13 such ascent is gradual and noticeable only in the layers away from the lower boundary ($\theta_0 > 290$ K). In contrast, in IOP14 the cross-isentropic ascent is more intense and spans the whole troposphere from the surface up to the tropopause.

Figures 10(c, d) show θ changes for the bin $300 < \theta_0 \leq 310$ [K] (cyan lines in Fig. 10(a,b)) in IOP13 and IOP14, respectively. The emergent structure is similar in both cases with the band top showing layers experiencing greatest heating. However, the heating intensity is very different between the two cases. In IOP13 the net heating attains a maximum near the end of the 21-h period barely reaching 10 K. In contrast, heating between 15 K and 20 K is reached in less than 10 hours into the simulation in IOP14.

Figure 11 shows the contributions to the θ changes in Figs. 10(c,d) from the four parametrized processes considered here. The BL and turbulent mixing parametrization is the main contributor in both cases (Fig. 11(a,e)). The convection parametrization starts contributing about five hours earlier in IOP14 than in IOP13 (Fig. 11(b,f)). Furthermore, this parametrization acts on a much wider layer in IOP14 than in IOP13, spanning from the 75th percentile up. This is consistent with the differences between cases in terms of convective activity, as described in Sections 4 and 5. The cloud microphysics parametrization in IOP14 starts contributing about two hours later than the convection parametrization in IOP14, but about nine hours earlier than the cloud microphysics parametrization in IOP13 (Fig. 11(c,g)). In the atmosphere, like in a numerical model, the main sources of heating are water phase changes. The three parametrization schemes that contribute to total heating do so mainly through latent heat release, including the BL and turbulent mixing parametrization. The latent heat release associated with the latter scheme can be found by tracing the changes in cloud liquid water and associated θ changes due to this parametrization (as in Martínez-Alvarado and Plant, 2014). In the atmosphere, unlike in a numerical model, phase changes are not distributed among parametrization schemes and the challenge for numerical models is to achieve the actual heating and induced cross-isentropic mass transport through the interaction between parametrization schemes and between the parametrization schemes and the dynamical core. These aspects are not always well represented by current numerical models (e.g. Martínez-Alvarado et al., 2015).

In general, the 2.5th-percentile lines in Fig. 10 describe slow cross-isentropic subsidence in both cyclones, corresponding to the widespread cross-isentropic subsidence discussed in Sections 4 and 5. This subsidence is associated with cooling. Figures 10(c,d) show that the lower part of the band with $300 < \theta_0 \leq 310$ [K] exhibits relatively weak cooling towards the end of the 21-h period in both cases. However, the cooling starts much earlier in IOP14 than in IOP13. The main parametrized process that contributes to cooling in IOP13 is radiation (Fig. 11d). Convection and cloud microphysics also contribute, but their contributions are less than 1 K each. In comparison, there are only two processes that contribute to cooling in IOP14, namely cloud microphysics (Fig. 11g) and radiation (Fig. 11h). Both processes have a relatively larger effect in IOP14 than in IOP13, as they occur over a wider layer and over a larger part of the sample in the former than in the latter.

The bin $300 < \theta_0 \leq 310$ [K] is shown because it exhibits strong cross-isentropic ascent while being away from the surface in both cyclones, providing fairer comparison conditions than a layer nearer the surface. However, each θ_0-bin is characterized by a different heating signature. This is particularly evident when comparing against an upper-troposphere θ_0-bin. For example, choosing the bin $320 < \theta_0 \leq 330$ [K], which is closer to the tropopause on average in both cases, results in a more important contribution of radiative cooling in both cases (not shown). In IOP13, the radiative contribution leads to weak cross-isentropic descent; in IOP14, the radiative contribution also leads to cross-isentropic descent in the lower part of the band, but it is balanced by contributions from cloud microphysics and convection which still manage to produce significant cross-isentropic ascent in the upper part of the band. This description is consistent with the behaviour followed by this θ_0 band in Figs. 10(a,b).

6.2 Circulation

In this section we follow the method described in Section 22.5 to compute the area-averaged isentropic vorticity ζ_θ and the contributions to ζ_θ associated with the materially-conserved and the diabatically-generated PV, $\zeta_{\theta,0}$ and $\zeta_{\theta,\mathrm{d}}$. The latter two are computed as

$$\zeta_{\theta,0} = \frac{1}{A}\int_R \sigma\, Q_0 dx\, dy \quad \text{and} \quad \zeta_{\theta,\mathrm{d}} = \frac{1}{A}\int_R \sigma\, Q_\mathrm{d} dx\, dy, \tag{18}$$

where $A = \int_R dx\, dy$.

When a large integration region (~ 1000 km) is used, the cyclones have similar vertical structures, an effect that has been noted in previous studies (e.g. Čampa and Wernli, 2012). When this is done for IOP13 and IOP14 at the end of 21-hour simulations, the ζ_θ profile is uniform vertically in both cases, corresponding to $\zeta_\theta \simeq 1.16f$ and $\zeta_\theta \simeq 1.25f$ in IOP13 and IOP14, respectively, where $f = 2\Omega \sin\phi$ is planetary vorticity, Ω is planetary angular speed and ϕ is latitude. This shows that, when these large length scales are considered, not only are the cyclones very similar to each other, but also the values of ζ_θ are close to the value that ζ_θ would have in an unperturbed atmosphere. Furthermore, the diabatic processes' contribution is small in both cases, apart from a low-level enhancement below 600 hPa in IOP14.

When smaller length scales are considered, the differences between cyclones are more apparent. The results corresponding to the last 18 hours in each simulation using, as integration regions, 500-km radius circles concentric to each cyclone are shown in Fig. 12. The cylindrical control volumes move with the cyclone center defined by minimum sea level pressure. These results are not qualitatively sensitive to the choice of radius, which has been confirmed by performing alternative analyses with 400-km and 600-km radii (not shown). The figure shows ζ_θ (black lines), the contribution from the materially-conserved PV (blue lines) and the total contribution from diabatic PV (orange lines) in IOP13 (upper row) and IOP14 (lower row). To provide an estimate of uncertainty due to the residual tracer r_Q, its contribution, computed as $\zeta_{\theta,\mathrm{r}} = \zeta_\theta - (\zeta_{\theta,0} + \zeta_{\theta,\mathrm{d}})$, has been added and subtracted from the conserved and diabatic tracers (dashed lines). The value of f at the position of the cyclone's center (gray lines) is also shown. All the computations have been carried out on isentropic surfaces, but to ease interpretation the results are also shown with pressure labelling the vertical coordinate. The indicated pressures correspond to the average pressure within the integration region at each isentropic level.

The IOP13 cyclone developed in a weakly cyclonic environment ($\zeta_\theta \simeq f$ at the start of the simulation; not shown). After three hours into the simulation ζ_θ is approximately vertically uniform with height and $\zeta_\theta \simeq 1.20f$ (Fig. 12a). As time passes, the ζ_θ profile remains constant up to around 500 hPa, level above which the ζ_θ values tend to increase slightly. Below the 500-hPa level ζ_θ increases slowly to reach a value at the end of the 21-h simulation of $\zeta_\theta \simeq 1.33f$ (Fig. 12d). This value is 15% larger than the value found when using a 1000-km radius circle as integration region. The diabatic contributions to the ζ_θ vertical profile in IOP13 developed over the first 15 hours of the simulation, which corresponds to 0300 UTC 18 July 2012 (Fig. 12c), after which a final state profile can be recognized. Positive diabatic contributions become important in the layer $450 < p < 650$ [hPa] (Fig. 12b) after the first nine hours of the simulation. Positive diabatic contributions then spread from that layer to lower levels, developing into a uniform contribution (Fig. 12c). Negative diabatic contributions are found at levels above 450 hPa, especially after the first fifteen hours of the simulation (Fig. 12c).

In contrast, the IOP14 cyclone developed in an already highly cyclonic environment ($\zeta_\theta > f$ at the start of the simulation), preconditioned by the presence of other low pressure systems in that same area (not shown). Thus, at the beginning of the 21-h study period ζ_θ was already large at mid-tropospheric levels. Three hours into the simulation the ζ_θ vertical profile is stratified into two layers (Fig. 12e). The lower layer (below 600 hPa) is characterized by $\zeta_\theta \simeq 1.47f$. Above 600 hPa, ζ_θ gradually increases with height to almost twice the value of f ($\zeta_\theta \simeq 1.87f$) around 500 hPa. This early profile then evolved during the following 18 hours into an approximately constant vertical profile with $\zeta_\theta \simeq 1.87f$ throughout (Fig. 12h). This value is 50% larger than the value found when using a 1000-km radius circle as isentropic integration area. In contrast to IOP13, the diabatic contributions to the ζ_θ vertical profile in IOP14 developed very rapidly, during the first nine hours of the simulation, into a final profile that only changed in intensity (Fig. 12f–h). Negative diabatic contributions were restricted to the layer $470 < p < 580$ [hPa]. Both, above and below that layer, diabatic processes contributed positively to ζ_θ. However, only in the lower layer the diabatic positive contributions clearly increased with time.

A property of the diabatic PV tracers is that the gain in the contribution due to diabatic processes across a given isentropic surface will always be balanced by a reduction in the contribution due to the Q_0 tracer and vice versa, except where the isentropic surface intersects orography. This property can be demonstrated as follows. In isentropic coordinates, (2) and (3) for Q_0 and Q_d, respectively, take the form

$$\frac{DQ_0}{Dt} = 0 \quad \text{and} \quad \frac{DQ_\mathrm{d}}{Dt} = -\frac{1}{\sigma}\nabla_\theta \cdot \boldsymbol{\mathcal{J}}_{\boldsymbol{F},\dot{\theta}}, \tag{19}$$

where ∇_θ is the gradient operator in isentropic coordinates and

$$\boldsymbol{\mathcal{J}}_{\boldsymbol{F},\dot{\theta}} = \left(\frac{\partial \theta}{\partial z}\right)^{-1} \boldsymbol{J}_{\boldsymbol{F},\dot{\theta}}, \tag{20}$$

where $\boldsymbol{J}_{\boldsymbol{F},\dot{\theta}} = -\dot{\theta}\,\nabla \times \boldsymbol{u}_\mathrm{a} - \boldsymbol{F} \times \nabla\theta$ (with components expressed in isentropic coordinates) is the non-advective part of the PV flux associated with the material rate of change of θ, $\dot{\theta} = D\theta/Dt$, and the frictional or other arbitrary force per unit mass exerted on the air, $\boldsymbol{F}$.

Using (19), the flux form of the PV equation (e.g. Haynes and McIntyre, 1987)

$$\frac{\partial(\sigma Q)}{\partial t} + \nabla_\theta \cdot \boldsymbol{\mathcal{J}} = 0 \tag{21}$$

can be split into two parts:

$$\frac{\partial(\sigma Q_0)}{\partial t} + \nabla_\theta \cdot \boldsymbol{\mathcal{J}}_0 = 0 \quad \text{and} \quad \frac{\partial(\sigma Q_\mathrm{d})}{\partial t} + \nabla_\theta \cdot \boldsymbol{\mathcal{J}}_\mathrm{d} = 0, \tag{22}$$

where

$$\boldsymbol{\mathcal{J}}_0 = \sigma Q_0 \boldsymbol{u}_\theta \quad \text{and} \quad \boldsymbol{\mathcal{J}}_\mathrm{d} = \sigma Q_\mathrm{d} \boldsymbol{u}_\theta + \boldsymbol{\mathcal{J}}_{\boldsymbol{F},\dot{\theta}}, \tag{23}$$

$\boldsymbol{u}_\theta = (u, v, \dot{\theta})$ is the three-dimensional wind velocity in isentropic coordinates and

$$\boldsymbol{\mathcal{J}} = \boldsymbol{\mathcal{J}}_0 + \boldsymbol{\mathcal{J}}_\mathrm{d}. \tag{24}$$

Haynes and McIntyre (1987) showed that the flux $\boldsymbol{\mathcal{J}}$ always lies on isentropic surfaces, i.e. its cross-isentropic component $\mathcal{J} = 0$. In contrast, the fluxes in (23) do not lie on isentropic surfaces unless the motion is adiabatic. Their cross-isentropic components are given by

$$\mathcal{J}_0 = \sigma Q_0 \dot{\theta}, \tag{25}$$

and

$$\mathcal{J}_{\mathrm{d}} = \sigma Q_{\mathrm{d}} \dot{\theta} + \mathcal{J}_{\boldsymbol{F},\dot{\theta}}. \tag{26}$$

Equation (25) makes the influence of diabatic processes on the evolution of Q_0 explicit. Under adiabatic conditions Q_0 will be simply redistributed isentropically. Since the cross-isentropic component of (24) is zero, we have that

$$\mathcal{J}_{\boldsymbol{F},\dot{\theta}} = -\sigma Q \dot{\theta}. \tag{27}$$

Recall however that, given (20), Q_{d} can still be modified by frictional forces under adiabatic conditions, even though no cross-isentropic flux would take place. Substituting (27) into (26) yields

$$\mathcal{J}_{\mathrm{d}} = -\sigma Q_0 \dot{\theta} = -\mathcal{J}_0, \tag{28}$$

i.e. the cross-isentropic advection of Q_{d} is equal in magnitude, but opposite in sign to that of Q_0, just as it should be for Q to satisfy the PV impermeability theorem (Haynes and McIntyre, 1987).

The link with the circulation diagnostics (16) is made through the integration of (22) over a control volume, moving with the cyclone surface pressure minimum and bounded laterally by contour C, enclosing region R, and above and below by isentropic surfaces $\theta + d\theta/2$ and $\theta - d\theta/2$, where $d\theta$ is a θ differential. Application of the divergence theorem and the expansion of $\sigma Q_0 \dot{\theta}$ in a Taylor series around θ yield the following two equations:

$$\frac{\partial C_0}{\partial t} + \oint_C \sigma Q_0 (\boldsymbol{u}_\theta - \boldsymbol{U}_{\mathrm{B}}) \cdot \boldsymbol{n}\, dl + \int_R \frac{\partial(\sigma Q_0 \dot{\theta})}{\partial \theta} dS = 0, \tag{29}$$

$$\frac{\partial C_{\mathrm{d}}}{\partial t} + \oint_C \sigma Q_{\mathrm{d}} (\boldsymbol{u}_\theta - \boldsymbol{U}_{\mathrm{B}}) \cdot \boldsymbol{n}\, dl + \oint_C \boldsymbol{\mathcal{J}}_{\boldsymbol{F},\dot{\theta}} \cdot \boldsymbol{n}\, dl - \int_R \frac{\partial(\sigma Q_0 \dot{\theta})}{\partial \theta}\, dS = 0 \tag{30}$$

where dl is a line element on contour C and $\boldsymbol{n}$ is the outward-pointing unit vector normal to the contour and parallel to the isentropic surface θ. (29) and (30) are shown in a general form appropriate for a control volume with lateral boundary of any shape where points on the boundary move with velocity $\boldsymbol{U}_{\mathrm{B}}$ along an isentropic surface (following Methven, 2015). The second terms on the left-hand sides of (29) and (30) are along-isentropic (parallel to isentropic surfaces) advective flux terms and the last terms are the cross-isentropic flux terms. Notice that, by (28), the cross-isentropic flux terms only differ in sign between (29) and (30). The third term in (30) is the along-isentropic non-advective Q_{d} flux term, which accounts for the effects, parallel to isentropic surfaces, of diabatic processes and frictional forces on C_{d}.

Under the hydrostatic approximation the along-isentropic components of the non-advective PV flux are $(\dot{\theta}\partial v/\partial\theta, -\dot{\theta}\partial u/\partial\theta)$ (Haynes and McIntyre, 1987) and therefore it scales as $\dot{\theta}U/\Delta\theta$, where U is a horizontal velocity scale and $\Delta\theta$ is an appropriate depth in isentropic coordinates. Therefore, the along-isentropic non-advective Q_{d} flux term scales as $2\pi r_{\mathrm{C}}\,\dot{\theta}U/\Delta\theta$, assuming a circular contour of radius r_{C}. Noting that σQ can be written in the form $f(1+\mathrm{Ro})$, where the Rossby number, Ro, is given by the ratio of relative to planetary vorticity, the cross-isentropic flux term scales as $\pi r_{\mathrm{C}}^2(1+\mathrm{Ro})f\dot{\theta}/\Delta\theta$. Therefore, the ratio of the along-isentropic non-advective flux term to the cross-isentropic flux term in (30) scales as

$$\frac{\oint_C \boldsymbol{\mathcal{J}}_{\boldsymbol{F},\dot{\theta}}\cdot\boldsymbol{n}\,dl}{\int_R dS\,\partial(\sigma Q_0\dot{\theta})/\partial\theta} \sim \frac{\mathrm{Ro}}{1+\mathrm{Ro}} \tag{31}$$

where $\mathrm{Ro} = 2U/(fr_{\mathrm{C}})$. At large r_{C} ($\sim$ 1000 km) we expect small Ro and therefore the evolution of C_{d} will be largely determined by the cross-isentropic flux term. However, as r_{C} decreases towards the Rossby radius of deformation ($\sim$ 500 km) or below, we expect larger Ro and the along-isentropic non-advective diabatic effects can become more important. In the limit of large Ro, the terms are comparable in magnitude. The opposing rates of increase between $\zeta_{\theta,\mathrm{d}}$ and $\zeta_{\theta,0}$ observed in Fig. 12, are mainly due to the cross-isentropic flux term appearing with opposite sign in (29) and (30). However, the total variation of ζ_θ on a given layer is not determined through this effect, but by the along-isentropic advection of Q_0 and Q_{d} and the along-isentropic non-advective effects of frictional forces and diabatic processes. These contributions depend on the particular conditions of each event. In IOP13, the terms are in approximate balance, leading to small temporal changes of the ζ_θ vertical profile. In contrast, in IOP14, these terms are not balanced and the ζ_θ vertical profile experiences larger temporal changes.

To conclude this Section, the contributions from individual diabatic processes to the ζ_θ vertical profiles are investigated. Figures 13(a–d) show the evolution of these contributions in IOP13; Figs. 13(e–h) show the corresponding evolution in IOP14. The two cases exhibit some similarities. In both cases, the BL and turbulent mixing parametrization produces a strong positive contribution at low levels and a strong negative contribution at upper levels. This effect is consistent with the discussion in Sections 4 and 5, regarding a heating maximum due to the BL and turbulent mixing parametrization around the level of BL top, which induces positive PV modification underneath and negative PV modification above. Also in both cases, the cloud microphysics parametrization produces an almost opposite pattern to the pattern produced by the BL and turbulent mixing parametrization: a neutral to negative contribution at low levels and a strong positive contribution at upper levels. However, the similarities between cases are far exceeded by the dissimilarities. The vertical location and span of the contributions due to the BL and the cloud microphysics parametrization schemes largely depend on the case. The most important difference in location and span is found in the contribution due to the cloud microphysics parametrization. This contribution is largest above the 600-hPa level in IOP13 (Figs. 13(a–d)) while in IOP14 this contribution tends to be more uniform throughout the layer shown in the figure. Another important difference between IOP13 and IOP14 is due to the contribution from the convection parametrization. This contribution is very small in IOP13 and only becomes noticeable above 500 hPa after 0300 UTC 18 July (Fig. 13b). Above that level, this contribution is negative and consistent with the region of negative PV modification discussed in Section 4 (cf. Fig. 6b). In contrast, the contribution due to the convection parametrization is important even from the beginning of the simulation in IOP14 (Figs. 13(e–h)). This contribution determines important features such as the location and intensity of the diabatically-generated PV contribution in the layer where this is negative ($470 < p < 580$ [hPa], cf. Figs. 12(e–h)). Below that layer, the contribution from the convection parametrization becomes less important so that the contributions leading to positive values in the ζ_θ vertical profiles are due to the BL and turbulent mixing and cloud microphysics parametrization schemes.

7 Conclusions

To investigate the importance of diabatic processes in determining the intensity of summer extratropical cyclones, the diabatic contributions to the evolution of two such cyclones have been analyzed. The two cyclones occurred in the vicinity of the United Kingdom during the summer of 2012. Despite similarities in precipitation and cyclone stationarity, the cyclones represented very different synoptic conditions. The first cyclone, observed during the DIAMET IOP13, deepened down to a minimum central sea level pressure of 995 hPa. In contrast, the second cyclone, observed during the IOP14, was a much deeper cyclone, with a minimum central sea level pressure of 978 hPa. The analysis was performed through simulations performed with the MetUM enhanced with diabatic tracers of θ and PV. The simulations were compared with Met Office operational analysis charts, radar rainfall observations and dropsonde measurements. Although summer extratropical cyclones typically possess much weaker winds than winter cyclones, the observations showed that water vapor mass flow along the warm conveyor belt of the stronger cyclone examined here was over half the magnitude of water vapor mass flow reported by other authors (e.g. Zhu and Newell, 1998) in wintertime atmospheric river cases where the cyclone and its warm conveyor belt move slowly. The large-scale environment was represented well by the model in both cases. However, when the water vapor mass flow rearwards relative to the motion of the cyclone is calculated for the weakest cyclone, the model overestimates the mass flow by approximately a factor of two. This is due to a greater flow and humidity extending above the boundary layer and deeper into the lower troposphere than observed. Despite these differences, consistent with a systematic wet bias in the model, the simulations provided a good representation of the mesoscale structure for at least 21 hours for IOP13 and 22 hours for IOP14.

The environment during IOP13 was colder and, therefore, had a lower saturation mixing ratio than the environment during IOP14. These contrasting environmental conditions led to weaker diabatic effects during IOP13 than during IOP14. The cyclone during IOP13 was characterized by a single column of large-scale ascent, corresponding to the system's WCB, and weak low-level positive PV anomalies. In contrast, the cyclone during IOP14 was characterized by a powerful WCB that wrapped in a spiral around and towards the cyclone's center forming several columns of large-scale ascent. Furthermore, this cyclone exhibited very strong positive PV anomalies, extending throughout the troposphere and constituting a PV tower.

In both cases, the low-level positive PV anomalies were diabatically produced. However, the amount of diabatic activity and the contribution from different parametrized processes were different in each case. In IOP13 the processes that contributed the most to the production of the low-level positive PV anomaly were the BL and turbulent mixing and cloud microphysics parametrization schemes. The convection parametrization also contributed to the production of the low-level positive PV anomaly in IOP14. The microphysics scheme gave rise to more positive PV within the WCB in both cases in the mid to upper troposphere and negative PV anomalies above this near the tropopause in the ridge wrapping above the bent back surface front. These anomalies are hypothesised to arise from latent heat release within upper tropospheric clouds. It is likely that condensation associated with saturated ascent dominates the PV anomalies associated with both the BL and turbulent mixing and cloud microphysics parametrizations.

Under the integral interpretation of diabatic θ tracers, the materially-conserved tracer θ_0 was used to label air masses for the analysis of cross-isentropic motion around the cyclones' centers. This analysis revealed striking differences in the cross-isentropic motion taking place in each cyclone. In IOP13 this motion was gradual (estimated maximum heating rate of 1 K h^{-1}) and mainly affected the layers in the middle part of the troposphere. In contrast, in IOP14 cross-isentropic motion was stronger (estimated maximum heating rate of 3 K h^{-1}) and virtually affected the whole troposphere. In both cases, heating was primarily produced by latent heat release through three parametrization schemes, namely BL and turbulent mixing, convection and cloud microphysics. The BL and turbulent mixing parametrization was the main contributor to total heating in both cyclones. However, the contribution from the BL and turbulent mixing scheme in IOP14 was 50% stronger than in IOP13. Furthermore, the convection parametrization contributed for longer and over a wider layer in IOP14 than in IOP13, confirming the importance of the convection parametrization in the development of the strongest cyclone. The radiation scheme mainly produced cooling in both cyclones. However, the magnitude of the radiation contribution was larger and affected a deeper layer in IOP14 than in IOP13. Stronger radiative cooling as well as stronger cooling due to cloud microphysics processes led to stronger cross-isentropic subsidence in IOP14 than in IOP13.

The use of the integral interpretation of diabatically-generated PV tracers in terms of area-averaged isentropic vorticity, ζ_θ, enabled the assessment of the effects of diabatic processes on the circulation around the cyclone center. Two effects were identified. First, while the vertical profile of ζ_θ remained approximately invariant in time for most of the considered period in IOP13, the corresponding profile in IOP14 changed throughout. Second, although the magnitude of PV in the PV tower in IOP14 grows rapidly through diabatic processes, this growth is not accompanied by an increase in the cyclone's absolute circulation at the same rate (a rather counter-intuitive result).

The explanation for both effects was found by applying the PV impermeability theorem (Haynes and McIntyre, 1987) to diabatic PV tracers. It was deduced that the ratio of the along-isentropic non-advective flux term to the cross-isentropic flux term in the equation of diabatically-generated circulation scales as $\mathrm{Ro}/(1+\mathrm{Ro})$. Therefore, it was shown that the cross-isentropic flux dominates the evolution of diabatically-generated circulation. Furthermore, it was shown that the impermeability of isentropic surfaces to PV fluxes implies the cancellation of the cross-isentropic flux of diabatically-generated PV by that of the materially-conserved PV in the evolution of total PV. Therefore, when considering the evolution of absolute circulation on an isentropic surface, the cross-isentropic flux has no effect. Instead, the PV flux (advective and non-advective) parallel to a given isentropic surface across the lateral boundary of a control volume becomes the only driver for the change of absolute circulation along that boundary on that isentropic surface. As a result, diabatic processes can lead to a large rate of change of diabatically-produced circulation and even to the development of a PV tower, such as in IOP14. Simultaneously, absolute circulation can exhibit a smaller rate of change, as in IOP14, or almost no change at all, as in IOP13. This result does not imply that latent heat release and other diabatic processes have no influence on the intensification of cyclones. It does mean though that we should consider the rate of intensification in terms of a moist baroclinic wave rather than attempting to understand an extratropical cyclone in isolation. In the framework introduced here, all the effects leading to cyclone intensification would be manifest as changes in the along-isentropic PV flux across the lateral boundaries of the control volume encompassing the cyclone core.

The analysis of these two contrasting summer cyclones has shown the suitability of diabatic tracers for the analysis of diabatic effects. Moreover, it has led to advances in the theory of diabatic tracers under the form of an integral interpretation. The integral interpretation of diabatic θ and PV tracers establishes a new framework for a systematic comparison of diabatic processes and their importance for the evolution of extratropical cyclones. This interpretation provides a quantitative way of measuring the effects of different diabatic processes, e.g. BL processes and mixing, convection and cloud microphysics, in a region rather than at a single point. Furthermore, the integral interpretation makes the tracers effectively independent of model resolution. A potential use of this property is the assessment of consistency between simulations at different resolutions, which is essential if truly seamless numerical weather and climate models are to be developed. Together with new observational techniques, including airborne measurements and satellite observations, the methods presented here can prove useful in answering questions such as what isentropic levels WCB outflows should reach (e.g. Martínez-Alvarado et al., 2014b), which is important in determining the effects on PV anomalies due to WCB outflows (Methven, 2015). Another related question is whether some modifiers of isentropic vorticity due to parametrized processes are missing in current numerical weather and climate models. The answers to these questions have implications for the development of new parametrizations of diabatic processes in numerical weather and climate models.

Acknowledgments

This work was initiated by the MSc dissertation of Ms Na Zhou, supervised by Profs Gray and Methven at the Department of Meteorology, University of Reading, and was funded by the United Kingdom's Natural Environment Research Council (NERC) as part of the DIAMET project (NE/I005234/1). The authors thank the following persons and organizations: Dr Jeffrey Chagnon, for useful discussion during the initial development of this work and, together with Mr Leo Saffin, for the implementation of PV tracers into the MetUM; Dr Christopher Dearden, for useful comments to the initial manuscript; two anonymous reviewers, for interesting and insightful comments that led to the improvement of the manuscript; the Met Office, for making the MetUM and associated initial and lateral boundary condition files available, and the NERC-funded National Centre for Atmospheric Science (NCAS)–Computational Modelling Services, for providing computing and technical support. The BAe-146 aircraft was flown by Directflight Ltd and managed by FAAM on behalf of NERC and the Met Office. Model output from the simulations of IOP13 and IOP14 is available through the NCAS British Atmospheric Data Centre (badc.nerc.ac.uk). The MetUM branches used are /dev/oma/vn7.3_thetra_residual/ revision number 15717 and /dev/LSaffin/vn7.3_PV_tracers_budget/ revision number 16506.

References

Adler, R., et al., 2003: The version 2 Global Precipitation Climatology Project (GPCP) monthly precipitation analysis (1979-present). *J. Hydrometeorol.*, **4**, 1147–1167.

Ahmadi-Givi, F., G. C. Craig, and R. S. Plant, 2004: The dynamics of a mid-latitude cyclone with very strong latent heat release. *Q. J. R. Meteorol. Soc.*, **130**, 295–323.

Browning, K. A. and N. M. Roberts, 1994: Structure of a frontal cyclone. *Q. J. R. Meteorol. Soc.*, **120**, 1535–1557.

Čampa, J. and H. Wernli, 2012: A PV perspective on the vertical structure of mature midlatitude cyclones in the Northern Hemisphere. *J. Atmos. Sci.*, **69**, 725–740.

Cavallo, S. M. and G. J. Hakim, 2009: Potential vorticity diagnosis of a tropopause polar cyclone. *Mon. Weather Rev.*, **137**, 1358–1371.

Chagnon, J. M. and S. L. Gray, 2009: Horizontal potential vorticity dipoles on the convective storm scale. *Q. J. R. Meteorol. Soc.*, **135**, 1392–1408.

Chagnon, J. M. and S. L. Gray, 2015: A diabatically-generated potential vorticity structure near the extratropical tropopause in three simulated extratropical cyclones. *Mon. Weather Rev.*, **143**, 2337–2347, doi:10.1175/MWR-D-14-00092.1.

Chagnon, J. M., S. L. Gray, and J. Methven, 2013: Diabatic processes modifying potential vorticity in a North Atlantic cyclone. *Q. J. R. Meteorol. Soc.*, **139**, 1270–1282.

Davies, T., M. J. P. Cullen, A. J. Malcolm, M. H. Mawson, A. Staniforth, A. A. White, and N. Wood, 2005: A new dynamical core for the Met Office's global and regional modelling of the atmosphere. *Q. J. R. Meteorol. Soc.*, **131**, 1759–1782.

Davis, C. A., 1992: A potential-vorticity diagnosis of the importance of initial structure and condensational heating in observed extratropical cyclogenesis. *Mon. Weather Rev.*, **120**, 2409–2428.

Dearden, C., G. Vaughan, T. Tsai, and J. P. Chen, 2016: Exploring the diabatic role of ice microphysical processes in UK summer cyclones. *Mon. Weather Rev.*, in press.

Dee, D. P., et al., 2011: The era-interim reanalysis: configuration and performance of the data assimilation system. *Q. J. R. Meteorol. Soc.*, **137**, 553–597.

Fu, Q., S. K. Krueger, and K. N. Liou, 1995: Interactions of radiation and convection in simulated tropical cloud clusters. *J. Atmos. Sci.*, **52**, 1310–1328.

Grams, C. M., et al., 2011: The key role of diabatic processes in modifying the upper-tropospheric wave guide: a North Atlantic case-study. *Q. J. R. Meteorol. Soc.*, **137**, 2174–2193.

Gray, S. L., 2006: Mechanisms of midlatitude cross-tropopause transport using a potential vorticity budget approach. *J. Geophys. Res.*, **111 (D17113)**, 14 pp, doi:10.1029/2005JD006259.

Hawcroft, M. K., L. C. Shaffrey, K. I. Hodges, and H. F. Dacre, 2012: How much northern hemisphere precipitation is associated with extratropical cyclones? *Geophys. Res. Lett.*, **39**, L24809.

Haynes, J. M., T. H. Vonder Haar, T. L'Ecuyer, and D. Henderson, 2013: Radiative heating characteristics of earth's cloudy atmosphere from vertically resolved active sensors. *Geophys. Res. Lett.*, **40**, 624–630.

Haynes, P. H. and M. E. McIntyre, 1987: On the evolution of vorticity and potential vorticity in the presence of diabatic heating and frictional or other forces. *J. Atmos. Sci.*, **44**, 828–841.

Huffman, G. J., R. F. Adler, M. M. Morrissey, D. T. Bolvin, S. Curtis, R. Joyce, B. McGavock, and J. Susskind, 2001: Global precipitation at one-degree daily resolution from multisatellite observations. *J. Hydrometeorol.*, **2**, 36–50.

Joos, H. and H. Wernli, 2012: Influence of microphysical processes on the potential vorticity development in a warm conveyor belt: a case-study with the limited-area model COSMO. *Q. J. R. Meteorol. Soc.*, **138**, 407–418.

Madonna, E., H. Wernli, H. Joos, and O. Martius, 2014: Warm conveyor belts in the ERA-Interim dataset (1979–2010). Part I: Climatology and potential vorticity evolution. *J. Clim.*, **27**, 3–26.

Martínez-Alvarado, O., L. H. Baker, S. L. Gray, J. Methven, and R. S. Plant, 2014a: Distinguishing the cold conveyor belt and sting jet air streams in an intense extratropical cyclone. *Mon. Weather Rev.*, **142**, 2571–2595.

Martínez-Alvarado, O., H. Joos, J. Chagnon, M. Boettcher, S. L. Gray, R. S. Plant, J. Methven, and H. Wernli, 2014b: The dichotomous structure of the warm conveyor belt. *Q. J. R. Meteorol. Soc.*, **140**, 1809–1824, doi:10.1002/qj.2276.

Martínez-Alvarado, O., E. Madonna, S. L. Gray, and H. Joos, 2015: A route to systematic error in forecasts of Rossby waves. *Q. J. R. Meteorol. Soc.*, in press.

Martínez-Alvarado, O. and R. S. Plant, 2014: Parameterised diabatic processes in numerical simulations of an extratropical cyclone. *Q. J. R. Meteorol. Soc.*, **140**, 1742–1755, doi: 10.1002/qj.2254.

Methven, J., 2015: Potential vorticity in warm conveyor belt outflow. *Q. J. R. Meteorol. Soc.*, **141**, 1065–1071.

Pedlosky, J., 1986: *Geophysical fluid dyanamics.* Springer, 710pp.

Rossa, A. M., H. Wernli, and H. C. Davies, 2000: Growth and decay of an extra-tropical cyclone's PV-tower. *Meteorol. Atmos. Phys.*, 139–156.

Saffin, L., J. Methven, and S. L. Gray, 2015: The non-conservation of potential vorticity by a dynamical core compared with the effects of parametrized physical processes. *Q. J. R. Meteorol. Soc.*, In press.

Schäfler, A. and F. Harnisch, 2015: Impact of the inflow moisture on the evolution of a warm conveyor belt. *Q. J. R. Meteorol. Soc.*, **141**, 299–310.

Shapiro, M. A. and D. Keyser, 1990: Fronts, jet streams and the tropopause. *Extratropical cyclones: The Erik Palmén Memorial Volume*, C. W. Newton and E. O. Holopainen, Eds., American Meteorological Society, Boston, USA, 167–191.

Simmons, A. J., S. Uppala, D. Dee, and S. Kobayashi, 2007: ERA-Interim: New ECMWF reanalysis products from 1989 onwards. *ECMWF Newsletter*, **110**, 25–35.

Stoelinga, M. T., 1996: A potential vorticity-based study of the role of diabatic heating and friction in a numerically simulated baroclinic cyclone. *Mon. Weather Rev.*, **124**, 849–874.

Tracton, M. S., 1973: The role of cumulus convection in the development of extratropical cyclones. *Mon. Weather Rev.*, **101**, 573–593.

Vaughan, G., 2011: Ensemble of atmospheric airborne and ground-based measurements including radar data from the DIAMET (DIAbatic influences on Mesoscale structures in ExTratropical storms) project, part of the Storms Risk Mitigation NERC research programme. NCAS British Atmospheric Data Centre, accessed: June 2014, `http://catalogue.ceda.ac.uk/uuid/6ca226c9634e57437f204ad9c5be77e1`.

Vaughan, G., et al., 2015: Cloud banding and winds in intense European cyclones – Results from the DIAMET Project. *B. Am. Meteorol. Soc.*, **96**, 249–265.

Whitehead, J. P., C. Jablonowski, J. Kent, and R. B. Rood, 2014: Potential vorticity: measuring consistency between GCM dynamical cores and tracer advection schemes. *Q. J. R. Meteorol. Soc.*, in Press.

Wilson, D. R. and S. P. Ballard, 1999: A microphysically based precipitation scheme for the UK Meteorological Office Unified Model. *Q. J. R. Meteorol. Soc.*, **125**, 1607–1636.

Zhu, Y. and R. E. Newell, 1998: A proposed algorithm for moisture fluxes from atmospheric rivers. *Mon. Weather Rev.*, **126**, 725–735.

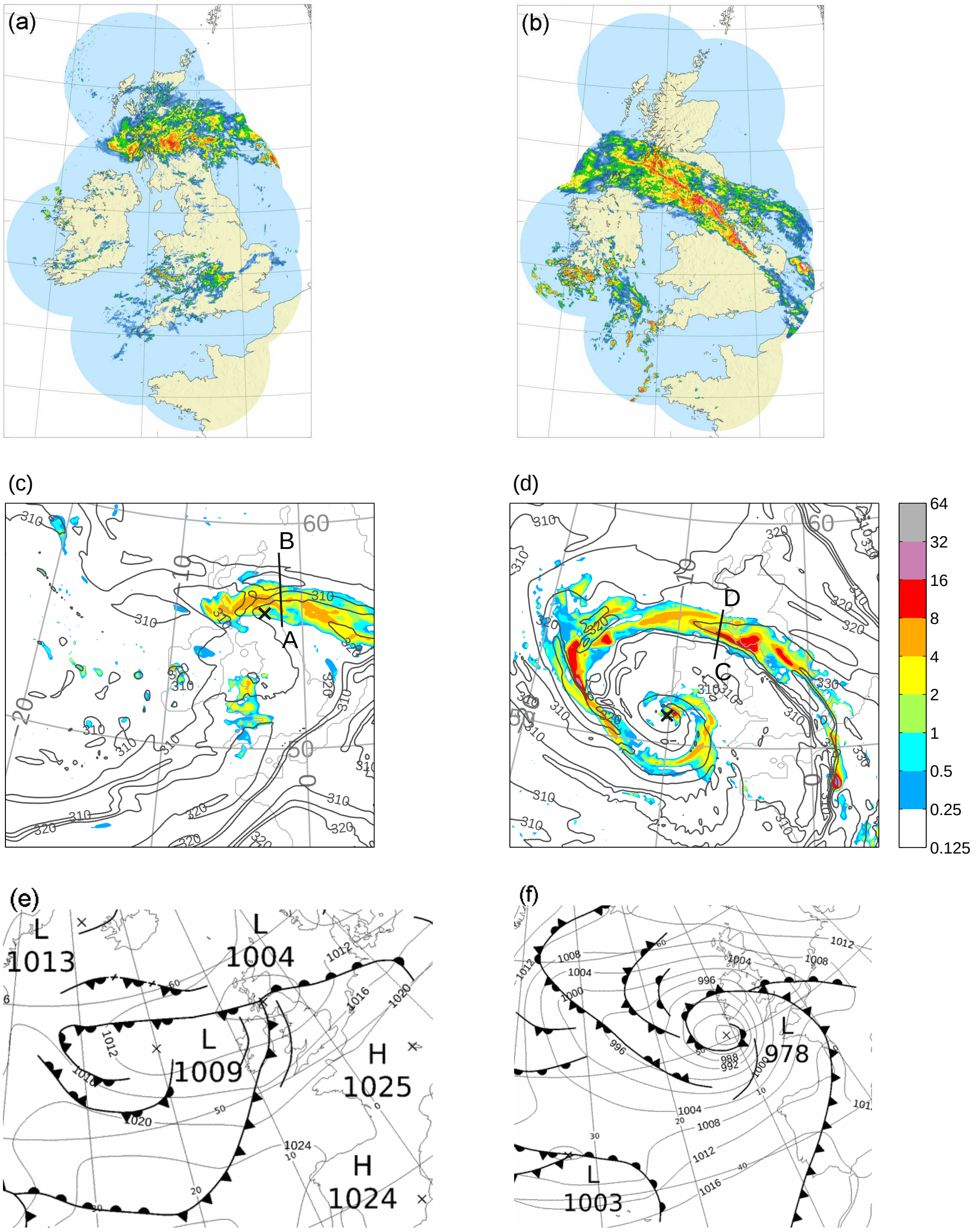

Figure 1: **(a,b)** Radar rainfall rates (courtesy Met Office ©2012 Crown Copyright) and **(c,d)** model-derived rainfall rates at **(a,c)** 0900 UTC 18 July 2012 and **(b,d)** 1600 UTC 15 August 2012. The colorbar on the right of **(d)** is also valid for **(a,b,c)**. In **(c,d)**, thin lines represent contours of 850-hPa equivalent potential temperature, in K and with a separation of 5 K, and the bold X represents the position of the low-pressure center while the segments A–B and C–D indicate the approximate position of dropsonde curtains. Synoptic charts at **(e)** 0600 UTC 18 July 2012 and **(f)** 1200 UTC 15 August 2012 (courtesy Met Office ©2012 Crown Copyright).

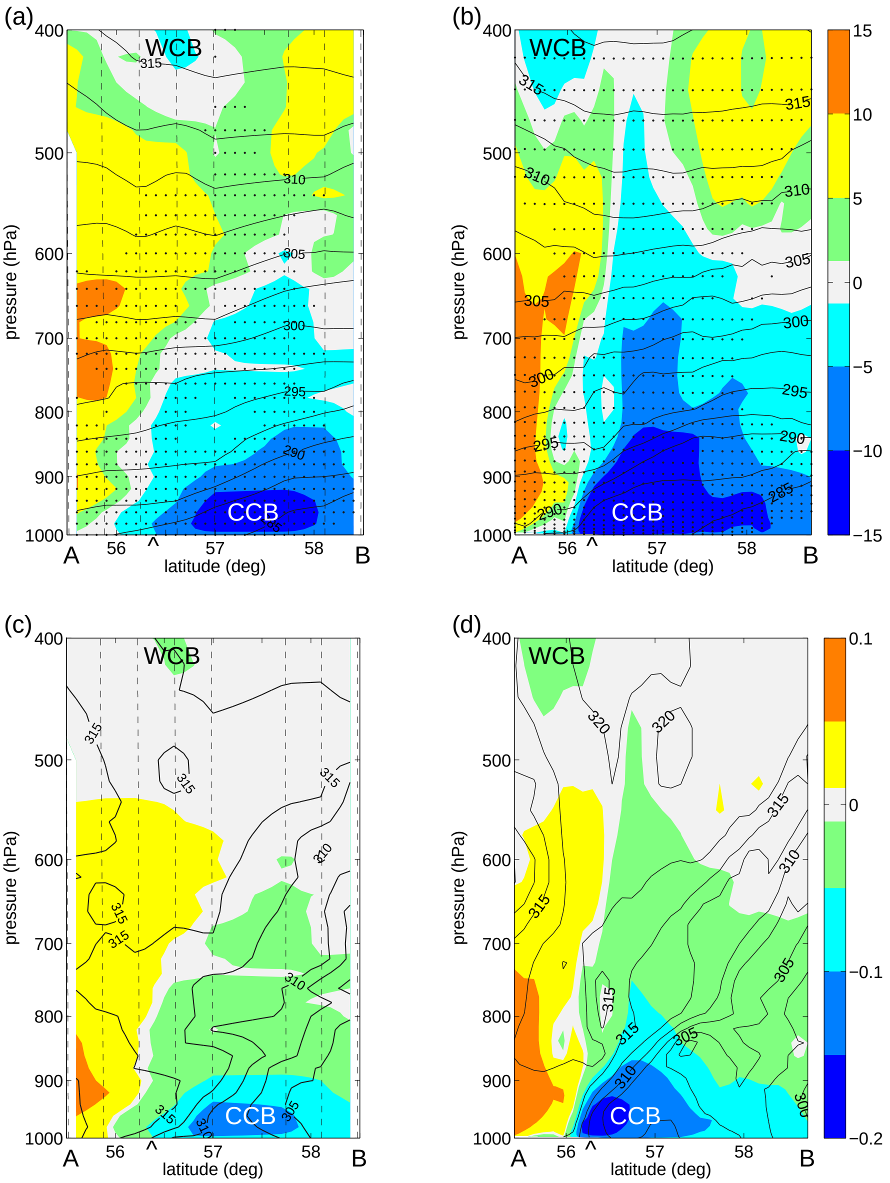

Figure 2: Vertical section along segment A–B in Fig. 1c showing in color shading **(a,b)** zonal velocity, in m s^{-1}, and **(c,d)** water vapor flux, in kg m^{-2} s^{-1}, at 0900 UTC 18 July 2012 (IOP13) derived from **(a,c)** dropsonde observations and **(b,d)** model output (T+21). In **(a,b)**, thin black lines represent potential temperature, in K, with a separation of 2.5 K; stippled areas indicate areas where relative humidity with respect to ice is larger than 90%. In **(c,d)**, thin black lines represent equivalent potential temperature contours, in K, with a separation of 2.5 K. Thin dashed lines in **(a,c)** represent dropsonde paths. The wedges mark the position of the surface front. WCB and CCB mark the position of the warm and cold conveyor belts, respectively.

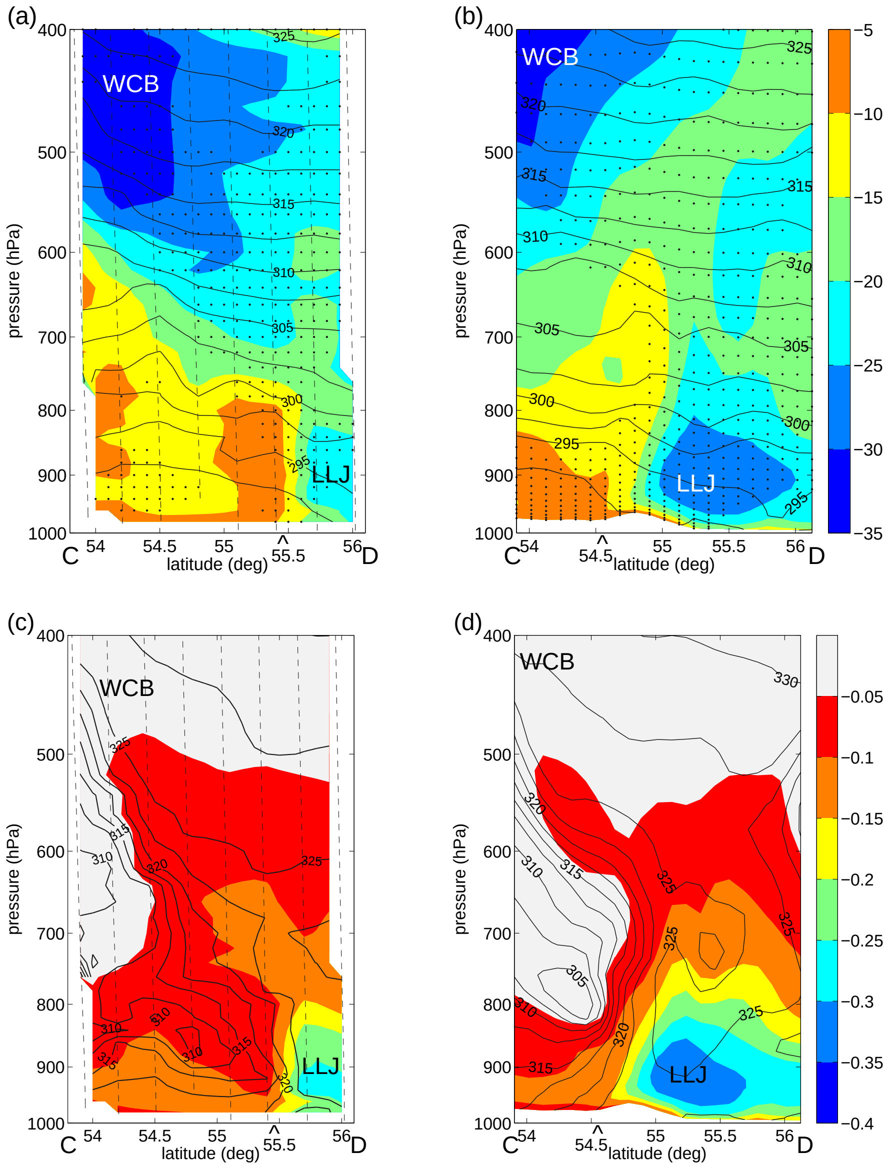

Figure 3: As in Fig. 2, but for the vertical section along segment C–D in Fig. 1d at 1600 UTC 15 August 2012 (IOP14). The model output in **(b,d)** corresponds to the output of 22-h integration. LLJ marks the position of a low-level jet. Notice that the colorbars in Fig. 2 and here are different.

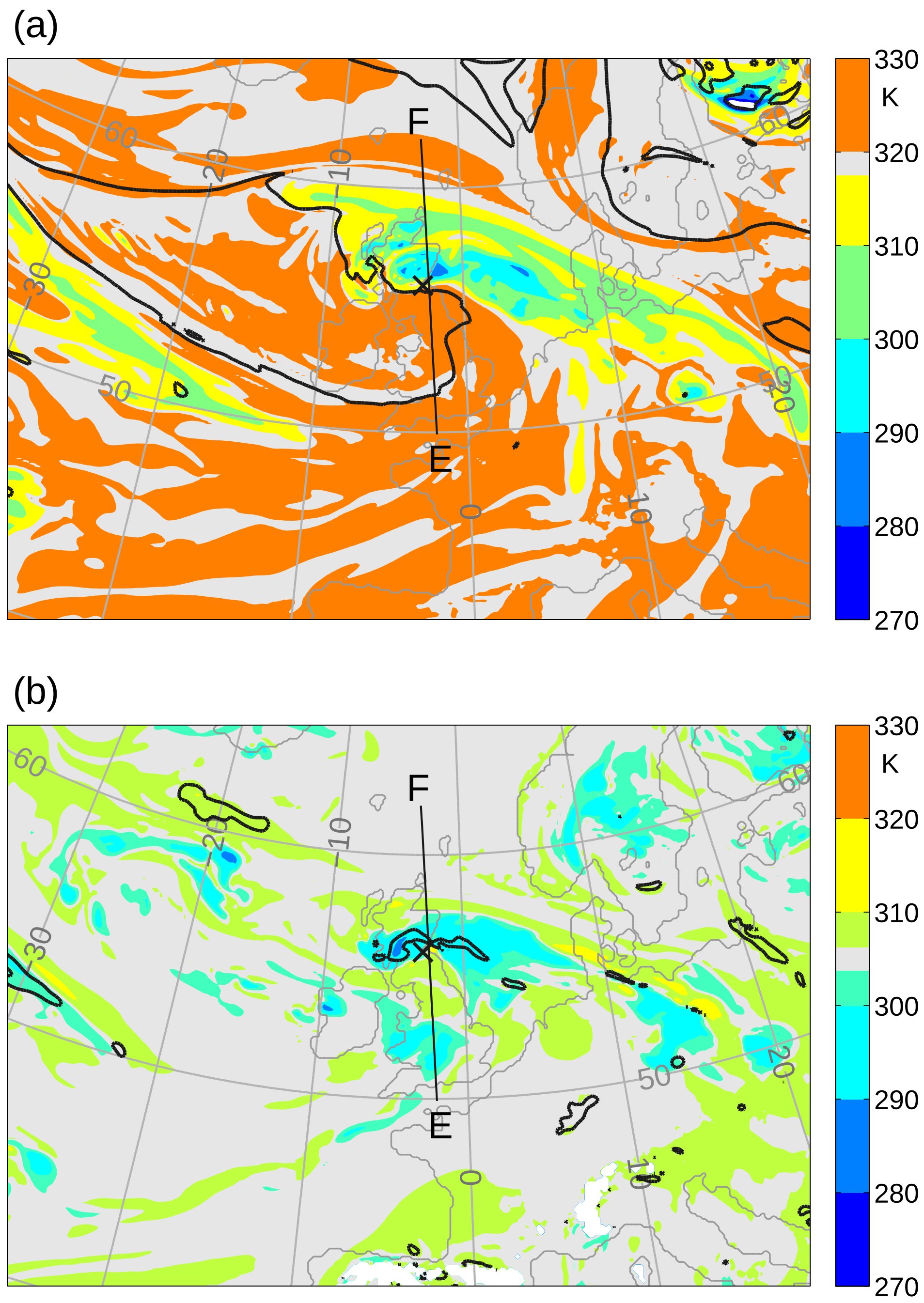

Figure 4: Maps of θ_0 tracer (color shading) at 0900 UTC 18 July 2012 (T+21, IOP13) at two isentropic levels: **(a)** 319 K and **(b)** 305 K. Bold black lines indicate 2-PVU PV contours at each isentropic level. The bold X represents the position of the low-pressure center and the segment E–F indicates the position of the sections in Figs. 5 and 6. White regions represent regions where the isentropic surfaces are not defined.

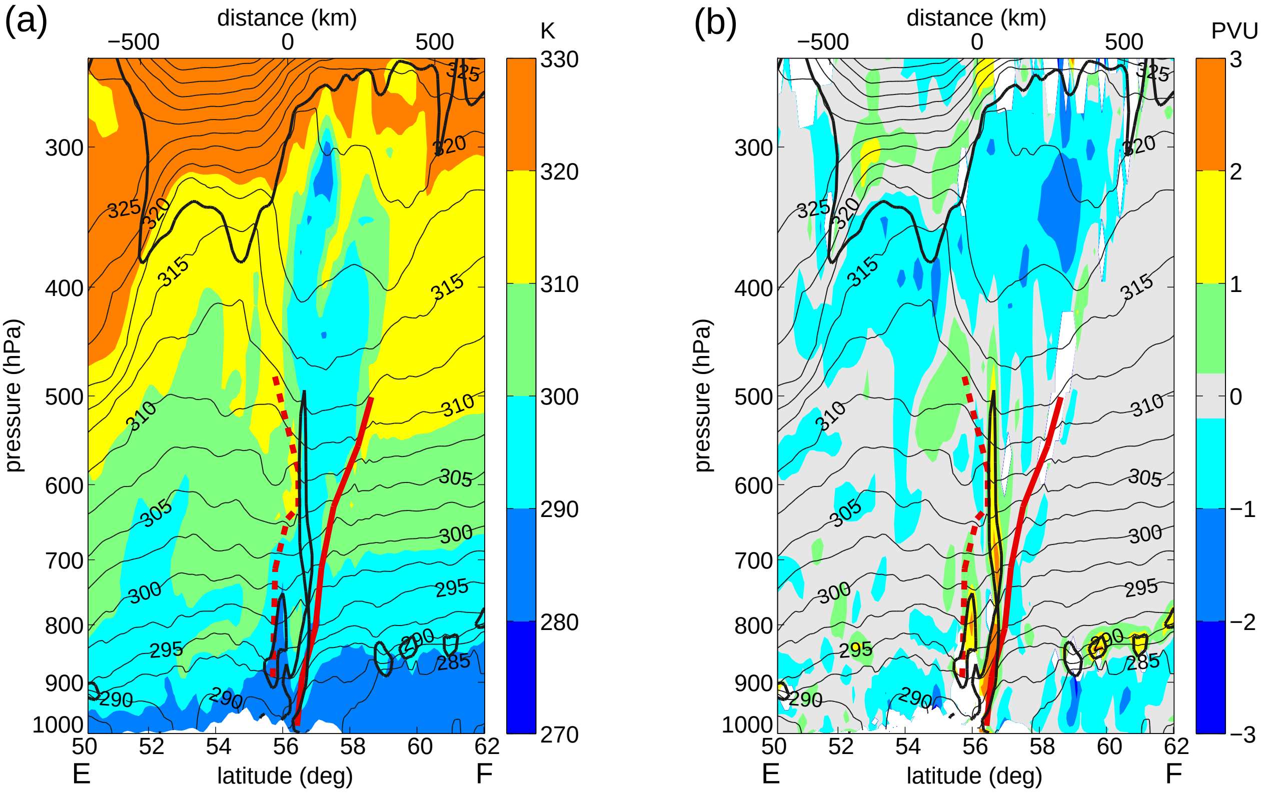

Figure 5: Vertical section along segment E–F in Fig. 4 showing in color shading **(a)** θ_0 and **(b)** total PV modification after 21 hours of integration at 0900 UTC 18 July 2012 (T+21, IOP13). In **(b)**, grid points where PV residual error is larger than 1 PVU or relative PV residual error is larger than 50% have been masked out (white shading). Thin black lines indicate potential temperature contours, in K, with a separation of 2.5 K. Bold black lines indicate 2-PVU PV contours. Bold red lines indicate the position of the system's warm (solid) and cold (dashed) fronts. The distance in the upper horizontal axis is the distance to the cyclone's center.

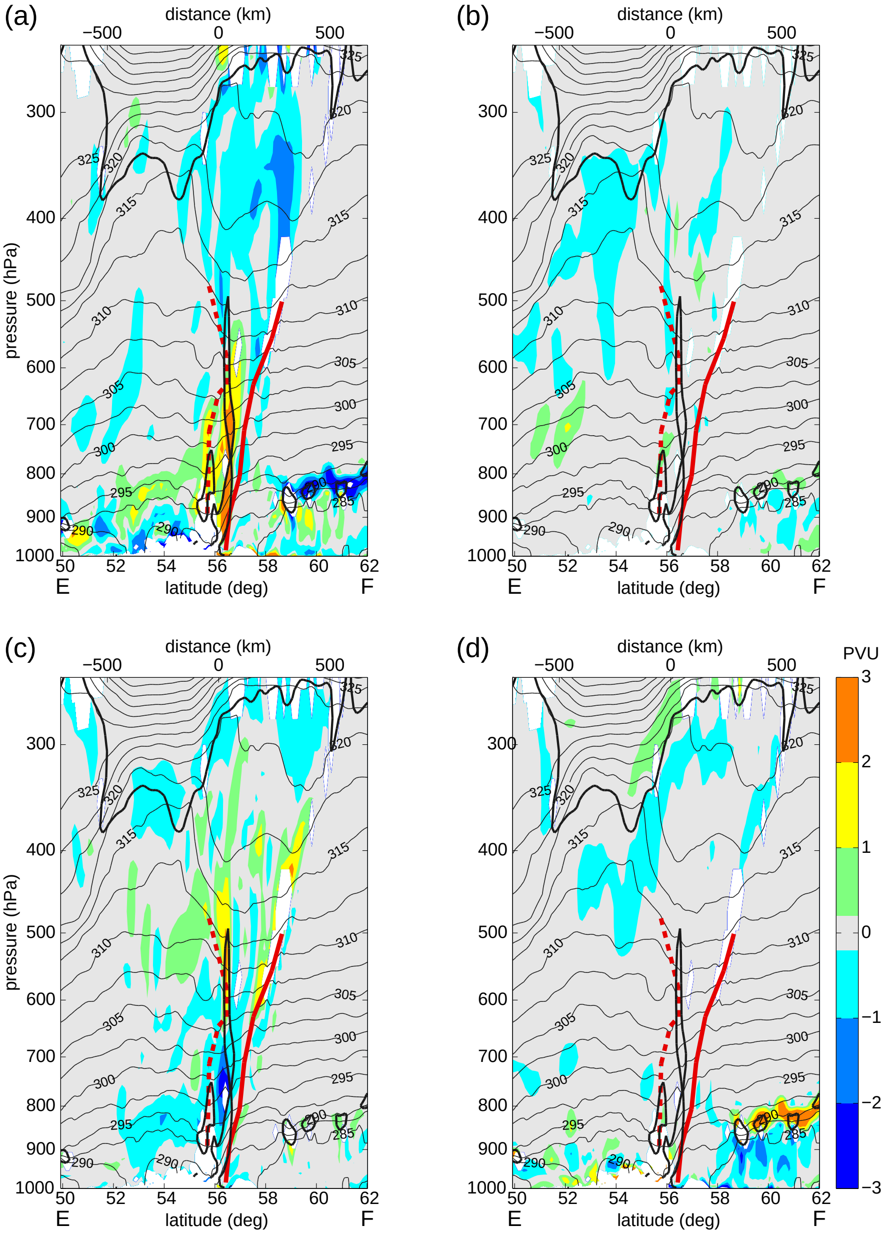

Figure 6: Vertical section along segment E–F in Fig. 4 showing in color shading contributions to PV modification from **(a)** BL and turbulent mixing, **(b)** convection, **(c)** cloud microphysics and **(d)** radiation after 21 hours of integration at 0900 UTC 18 July 2012 (T+21, IOP13). Grid points where PV residual error is larger than 1 PVU and relative PV residual error is larger than 50% have been masked out. Thin black lines indicate potential temperature contours, in K, with a separation of 2.5 K. Bold black lines indicate 2-PVU PV contours. Bold red lines indicate the position of the system's warm (solid) and cold (dashed) fronts.

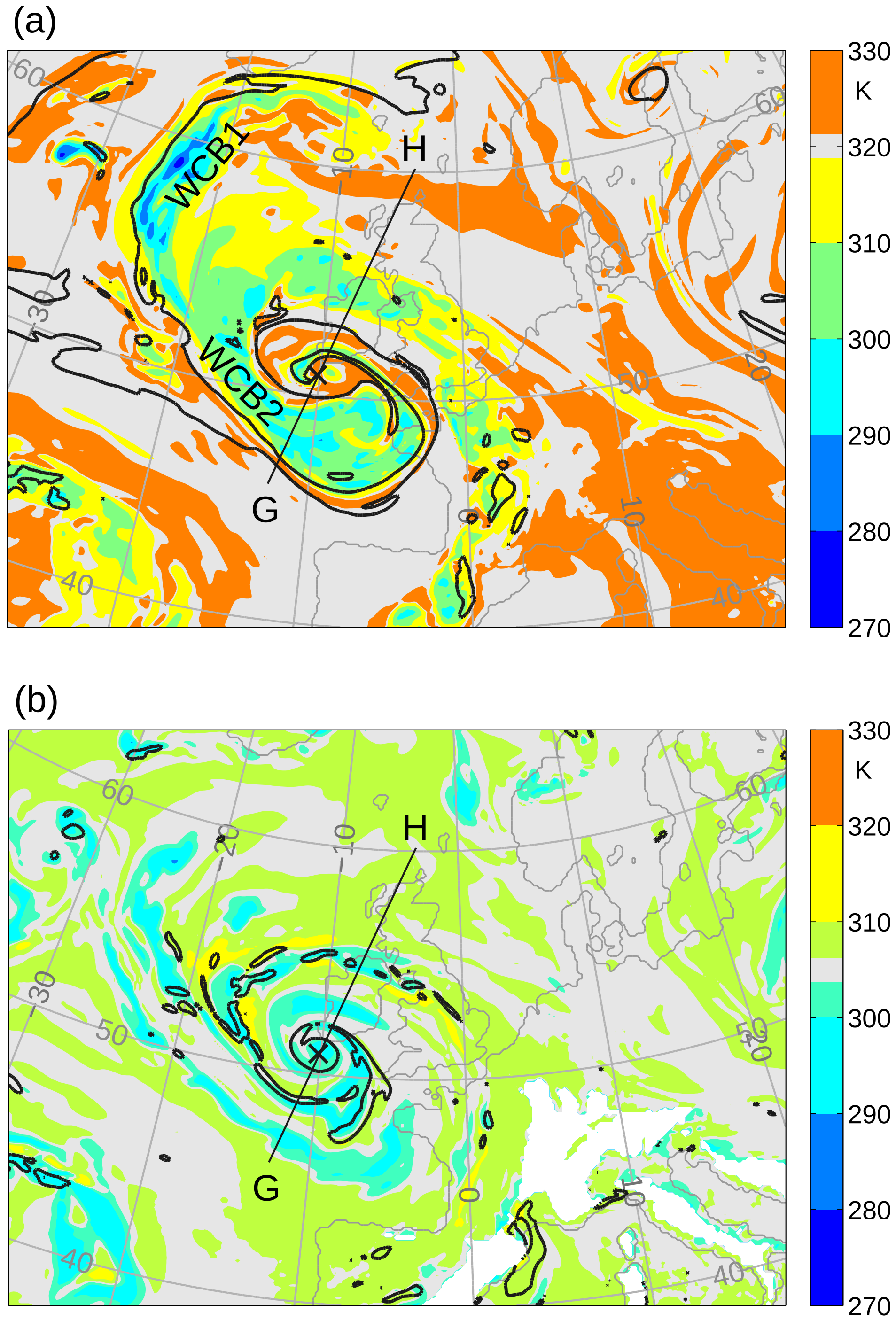

Figure 7: As in Fig. 4, but for IOP14 at 1500 UTC 15 August 2012 (T+21) at the isentropic levels **(a)** 320 K and **(b)** 305 K. The segment G–H indicates the position of the vertical sections in Figs. 8 and 9. WCB1 and WCB2 indicate the primary and secondary WCB branches, respectively.

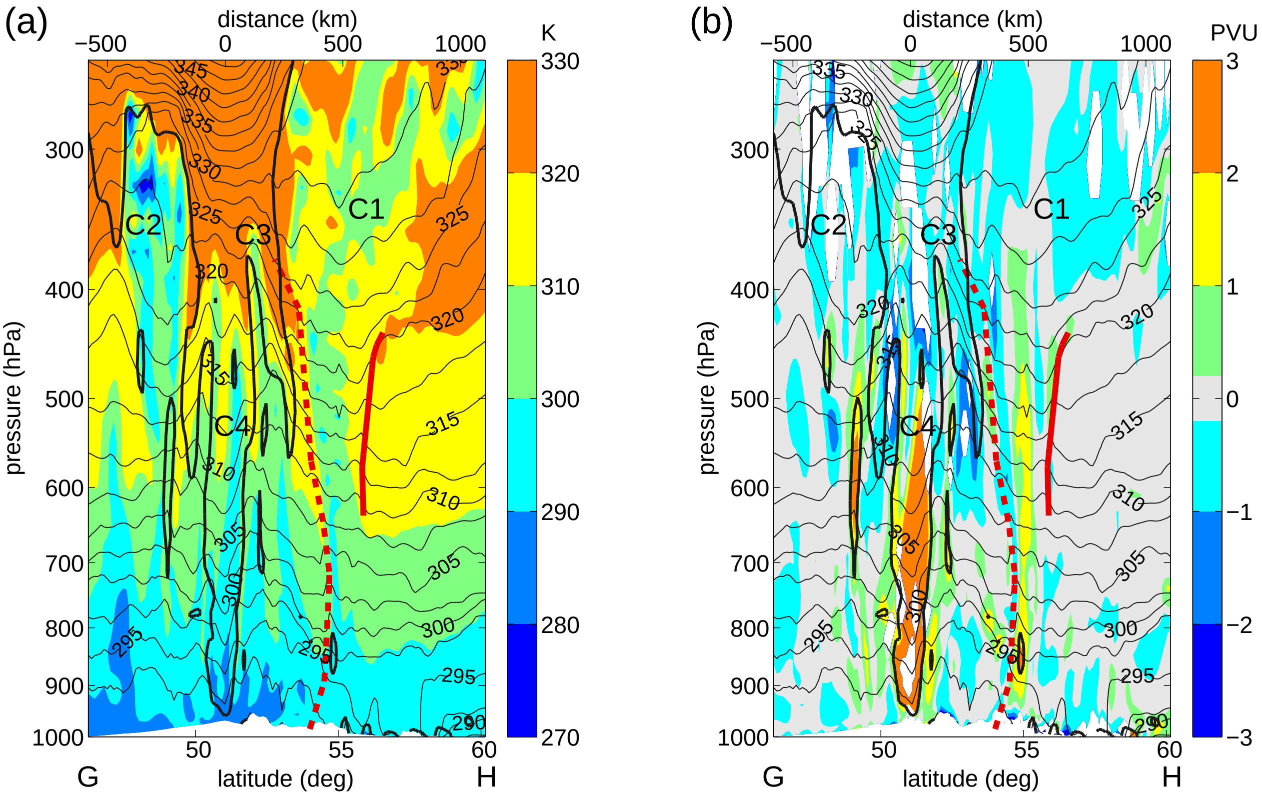

Figure 8: As in Fig. 5, but for the vertical section along segment G–H in Fig. 7 at 1500 UTC 15 August 2012 (T+21, IOP14). Bold red lines indicate the position of the system's occluded warm (solid) and surface cold (dashed) fronts. Labels C1, C2 and C3 indicate the position of columns of cross-isentropic ascent. Label C4 indicates the position of a PV tower.

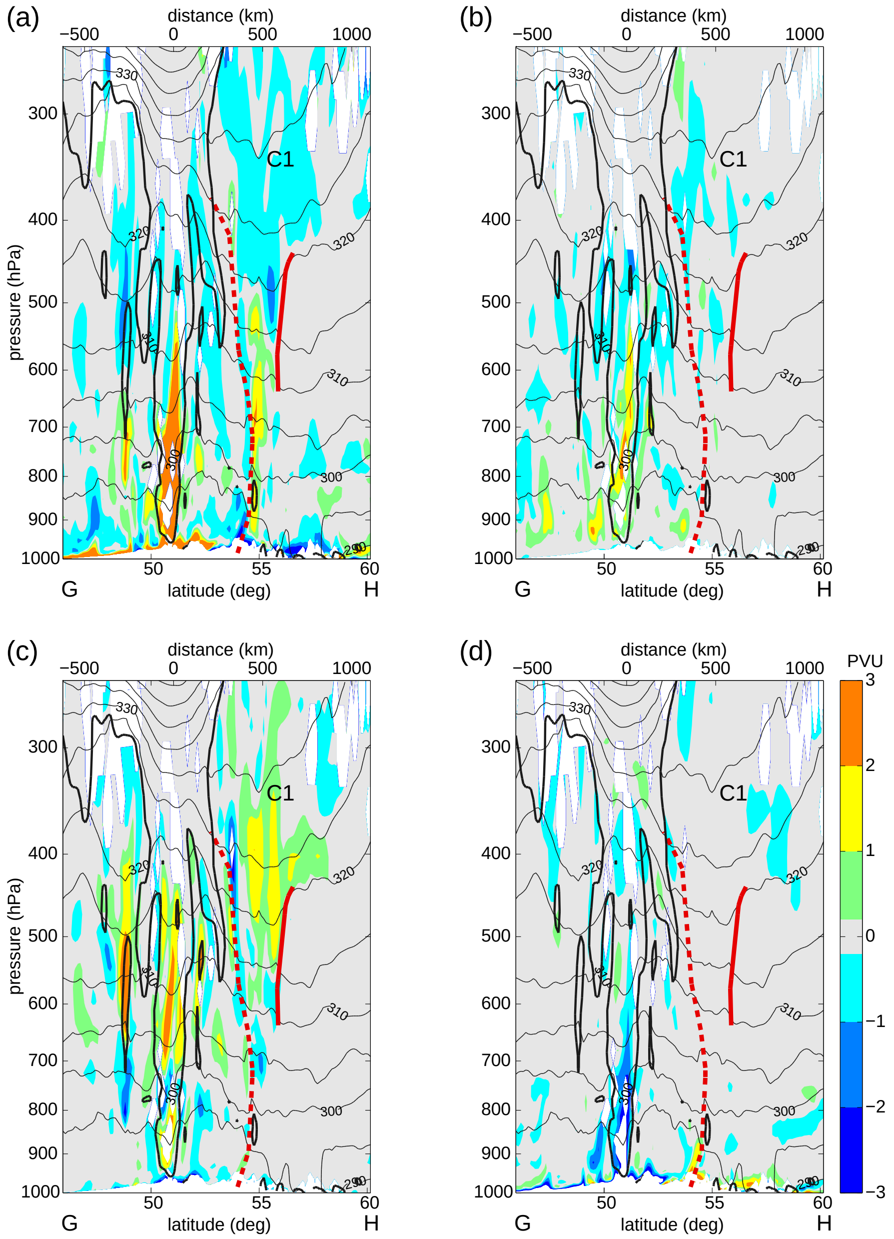

Figure 9: As in Fig. 6, but for the vertical section along section G–H in Fig. 7 at 1500 UTC 15 August 2012 (T+21, IOP14). Bold red lines indicate the position of the system's occluded warm (solid) and surface cold (dashed) fronts. Label C1 represents the position of the strongest column of cross-isentropic ascent.

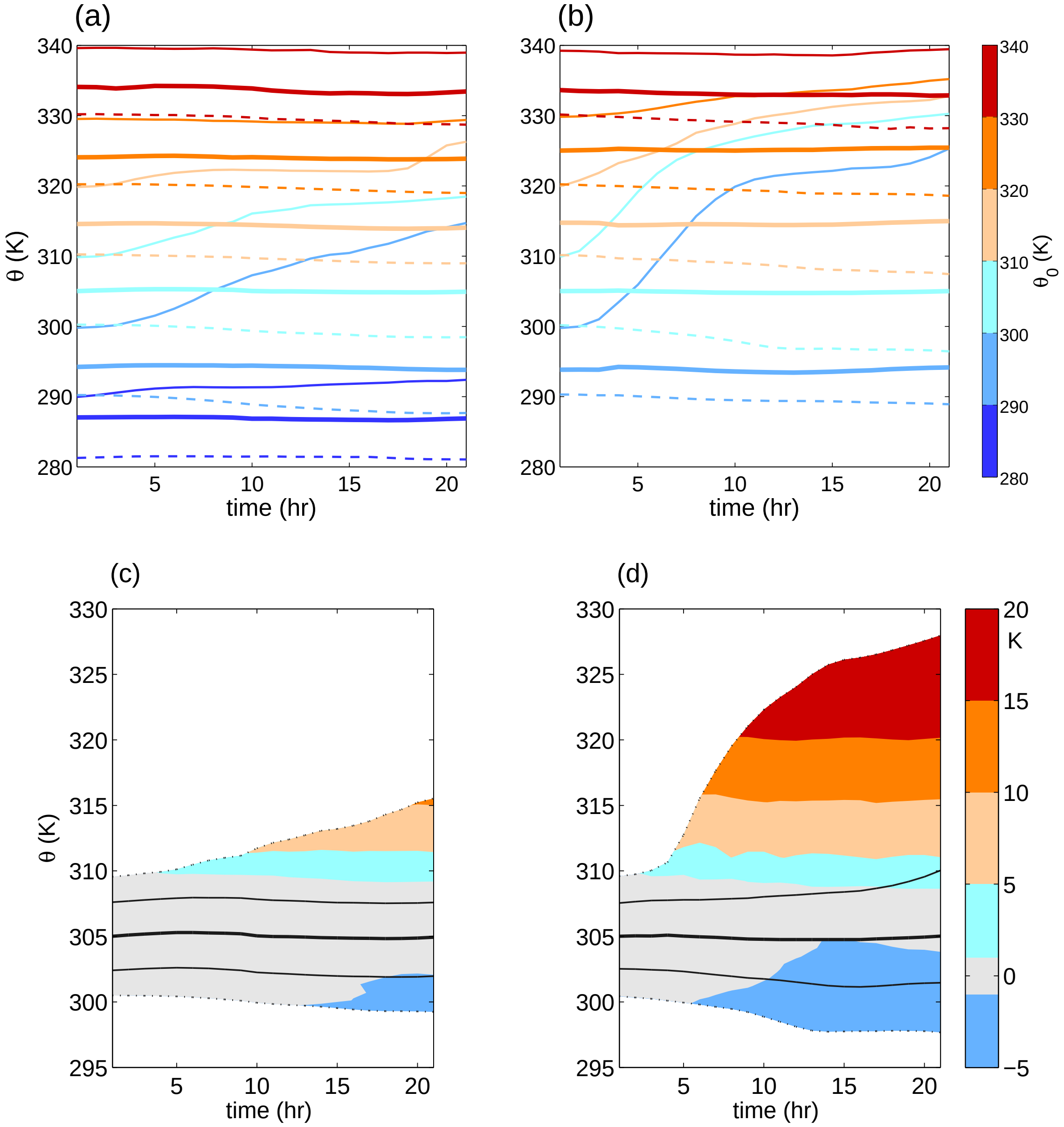

Figure 10: **(a,b)** Cross-isentropic mass transport within a 1000-km spherical cap concentric to the cyclone for **(a)** IOP13 and **(b)** IOP14. The lines are colored according to the θ_0-bin whose PDF they represent. Dashed lines, bold solid lines and thin solid lines represent the 2.5$^{\text{th}}$, 50$^{\text{th}}$ and 97.5$^{\text{th}}$ percentiles of θ values, respectively, identified within each θ_0-bin. **(c,d)** Heating in the bin with $300 < \theta_0 \leq 310$ [K] in a 1000-km spherical cap concentric to the cyclone for **(c)** IOP13 and **(d)** IOP14. Bold lines represent medians; thin lines represent the 25$^{\text{th}}$ and 75$^{\text{th}}$ θ-value percentiles; dotted lines represent the 5$^{\text{th}}$ and 95$^{\text{th}}$ θ-value percentiles.

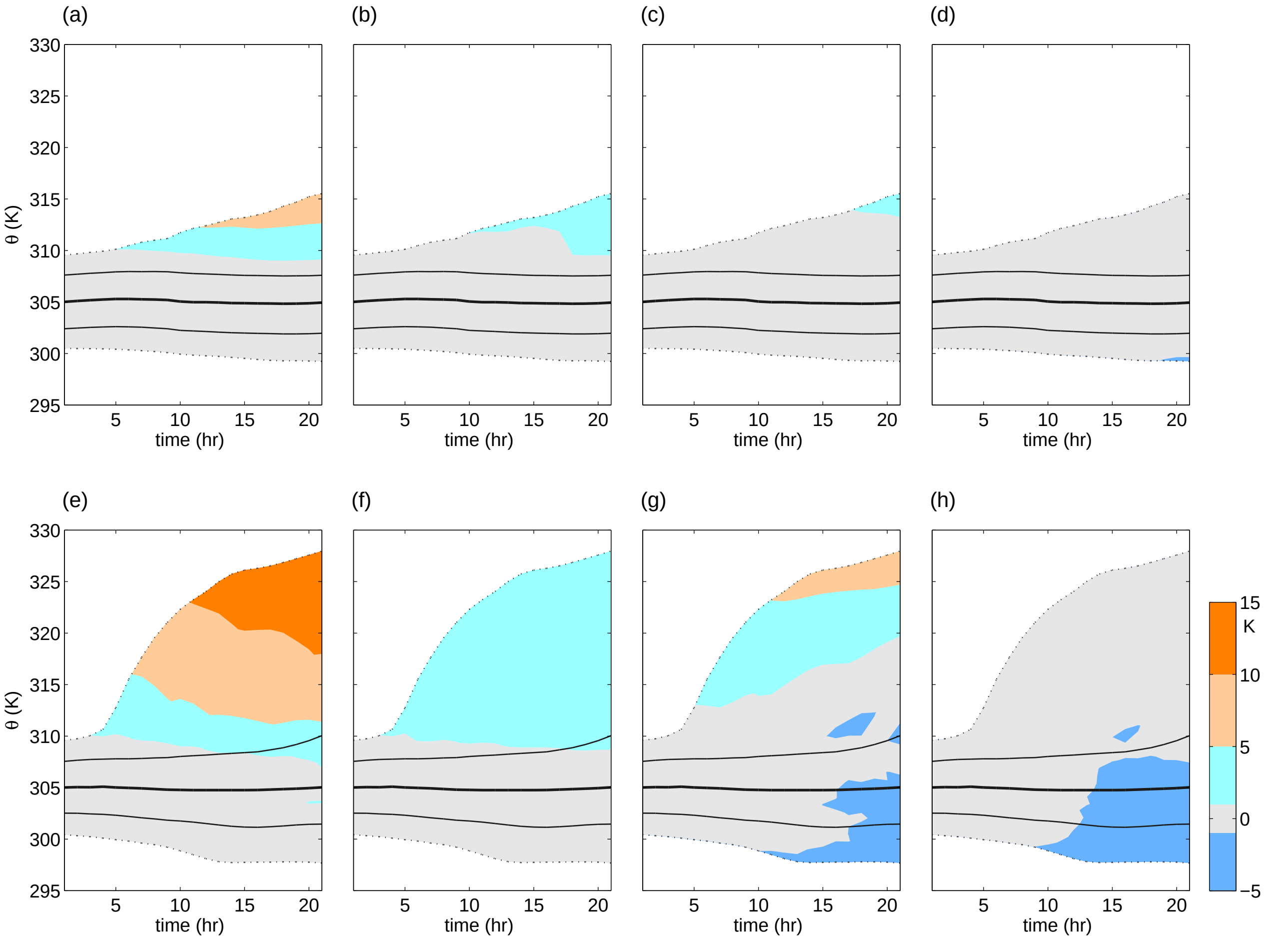

Figure 11: Heating due to the parametrization of **(a,e)** BL and turbulent mixing, **(b,f)** convection, **(c,g)** cloud microphysics and **(d,h)** radiation for the bin with $300 < \theta_0 \leq 310$ [K] in a 1000-km spherical cap concentric to the cyclone for **(a-d)** IOP13 and **(e-h)** IOP14. Bold lines represent medians; thin lines represent 25^{th} and 75^{th} θ-value percentiles; dotted lines represent 5^{th} and 95^{th} θ-value percentiles

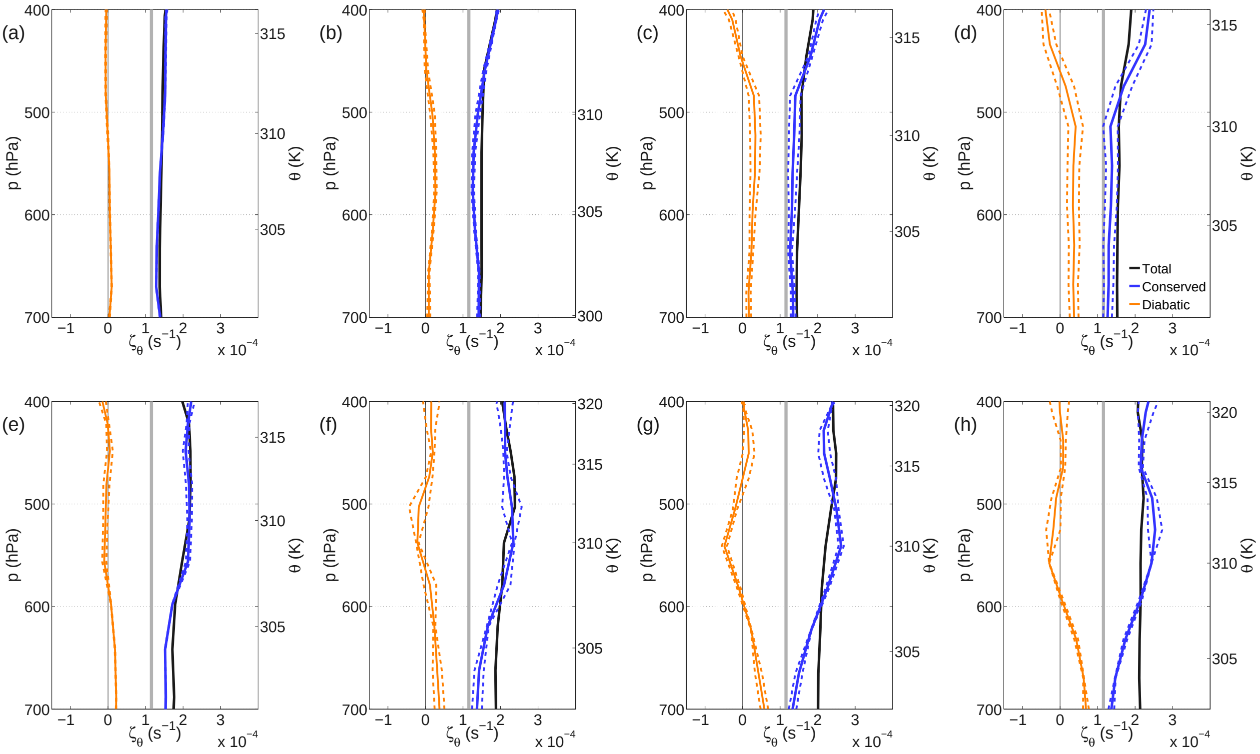

Figure 12: Vertical profiles of average isentropic vorticity (black) for a 500-km spherical cap concentric to the cyclone for **(a–d)** IOP13 and **(e–h)** IOP14: **(a)** 1500 UTC (T+3) and **(b)** 2100 UTC 17 July 2012 (T+9); **(c)** 0300 UTC (T+15) and **(d)** 0900 UTC 18 July 2012 (T+21); **(e)** 2100 UTC 14 August 2012 (T+3); **(f)** 0300 UTC (T+9); **(g)** 0900 UTC (T+15) and **(h)** 1500 UTC 15 August 2012 (T+21). The frames also show contributions from conserved PV (blue) and diabatically-generated PV (orange), and the value of planetary vorticity at the position of the cyclone's center (gray vertical line). The dashed lines represent the conserved and diabatically-generated PV contributions with the contribution from the residual added and subtracted as an indication of uncertainty.

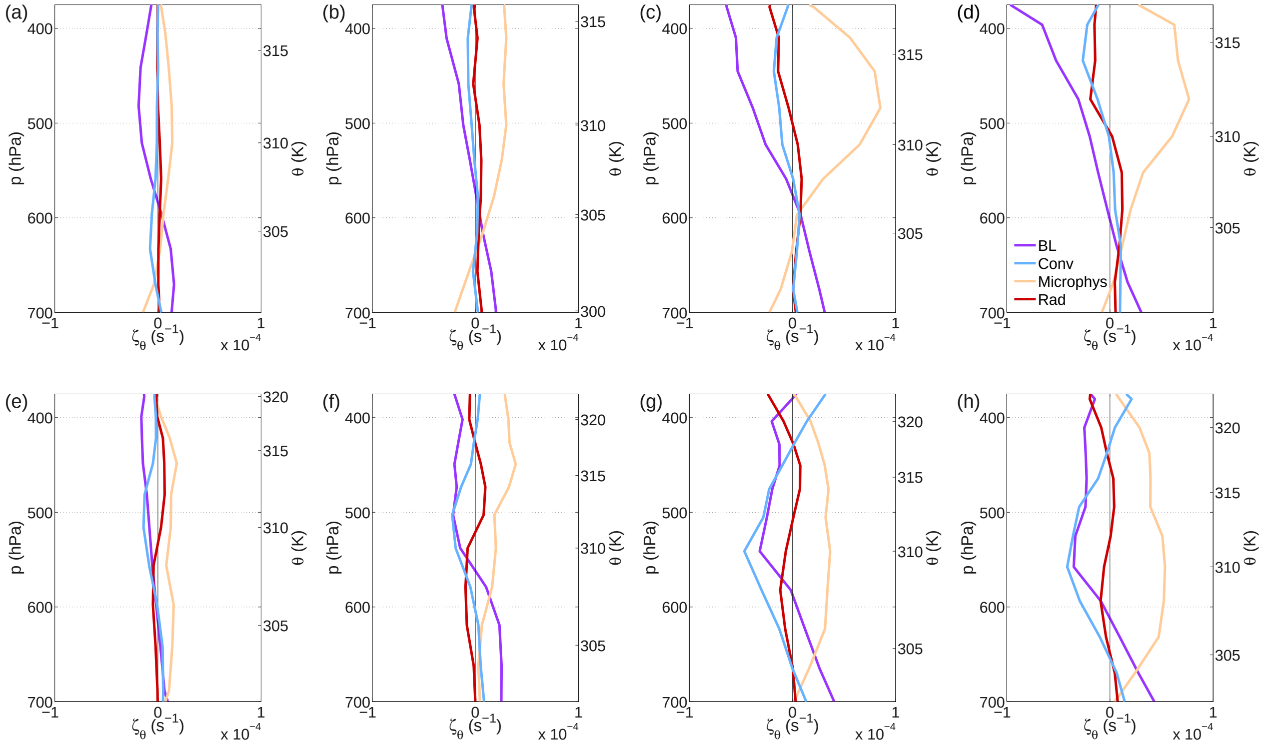

Figure 13: Vertical profiles of contributions of BL and turbulent mixing processes (BL), parametrized convection (Conv), cloud microphysics processes (Microphys) and radiation (Rad) to average isentropic vorticity for a 500-km spherical cap concentric to the cyclone for **(a–d)** IOP13 and **(e–h)** IOP14: **(a)** 1500 UTC (T+3) and **(b)** 2100 UTC 17 July 2012 (T+9); **(c)** 0300 UTC (T+15) and **(d)** 0900 UTC 18 July 2012 (T+21); **(e)** 2100 UTC 14 August 2012 (T+3); **(f)** 0300 UTC (T+9); **(g)** 0900 UTC (T+15) and **(h)** 1500 UTC 15 August 2012 (T+21).